



**Influence of the TiO₂ Electronic Structure and of Strong
Metal-Support Interaction on Plasmonic Au Photocatalytic
Oxidation**

Journal:	<i>Catalysis Science & Technology</i>
Manuscript ID	CY-ART-10-2015-001736.R1
Article Type:	Paper
Date Submitted by the Author:	n/a
Complete List of Authors:	<p>Naldoni, Alberto; Università degli Studi di Milano, Dipartimento di Chimica fisica ed Elettrochimica Riboni, Francesca; Università degli Studi di Milano, Dipartimento di Chimica marelli, marcello; CNR-ISTM, Bossola, Filippo; Università dell'Insubria, Dipartimento di Scienza e Alte Tecnologie Ulisse, Giacomo; University of Rome "Tor Vergata", Department of Electronic Engineering Di Carlo, Aldo; University of Rome Tor Vergata, Dept. Electronic Engineering Pis, Igor; Elettra-Sincrotrone Trieste S.C.p.A., S.S. 14 Km 163.5, I-34149 Basovizza, Nappini, Silvia; IOM-CNR, malvestuto, marco; Sincrotrone Trieste, Dozzi, Maria Vittoria; Università degli Studi di Milano, Dipartimento di Chimica Fisica ed Elettrochimica Psaro, Rinaldo; Univesita degli Studi di Milano, CNR Centre c/o Dip Chimica Inorganica Selli, Elena; Università degli Studi di Milano, Dipartimento di Chimica Fisica Dal Santo, Vladimiro; ISTM-CNR,</p>

Royal Society of Chemistry

Guidelines to Referees

Catalysis Science & Technology - www.rsc.org/catalysis

Catalysis Science & Technology is a multidisciplinary journal that focuses on both the fundamental science and technological aspects of catalysis. The journal aims to contain a mix of fundamental, applied, experimental and computational work, thus appealing to both academic and industrial scientists.

Catalysis Science & Technology has a 2014 impact factor of **5.43** and wishes to encourage very high quality papers reporting exciting new developments and the journal aims bring together the top research from the homogeneous, heterogeneous and bio-catalysis communities. For an article to be accepted it must report high quality new work and make a significant contribution to the field.

Routine or unnecessarily fragmented work, however competently researched and reported, should **not** be recommended for publication.

Communications must report high quality new work of sufficient importance and impact to justify preliminary publication.



General Guidance

When preparing your report, please:

- comment on the originality, importance, impact and scientific reliability of the work;
- state unequivocally whether you would like to see the paper accepted or rejected and give detailed comments (with references, as appropriate) that will both help the Editor to make a decision on the paper and the authors to improve it;
- do not make comments about the manuscript or authors which may cause offence.

For confidentiality reasons, please:

- treat the work and the report you prepare as confidential; the work may not be retained (in any form), disclosed, used or cited prior to publication; if you need to consult colleagues to help with the review, please inform them that the manuscript is confidential, and inform the Editor;
- do not communicate directly with authors; *NB* your anonymity as a referee will be strictly preserved from the authors.

Please inform the Editor if:

- there is a conflict of interest;
- there is a significant part of the work which you are not able to referee with confidence;
- if the work, or a significant part of the work, has previously been published, including online publication (e.g. on a preprint server/open access server);
- you believe the work, or a significant part of the work, is currently submitted elsewhere;
- the work represents part of an unduly fragmented investigation.

When submitting your report, please:

- provide your report rapidly and within the specified deadline, or inform the Editor immediately if you cannot do so;
- submit your report at <http://mc.manuscriptcentral.com/cy>.

For further details, see the RSC's Refereeing Procedure and Policy — www.rsc.org/pdf/authrefs/ref.pdf



Catalysis Science and Technology

ARTICLE

Influence of the TiO₂ Electronic Structure and of Strong Metal-Support Interaction on Plasmonic Au Photocatalytic Oxidations

Alberto Naldoni,^{a,†} Francesca Riboni,^{b,‡,†} Marcello Marelli,^a Filippo Bossola,^{a,c} Giacomo Ulisse,^d Aldo Di Carlo,^d Igor Piš,^{e,f} Silvia Nappini,^{e,f} Marco Malvestuto,^e Maria Vittoria Dozzi,^b Rinaldo Psaro,^a Elena Selli,^{b,*} and Vladimiro Dal Santo.^{a,*}

Received 00th January 20xx,
Accepted 00th January 20xx

DOI: 10.1039/x0xx00000x

www.rsc.org/

Aiming at understanding how plasmonic reactions depend on important parameters such as metal loading and strong metal-support interaction (SMSI), we report the plasmonic photodegradation of formic acid (FA) under green LED irradiation employing three TiO₂ supports (stoichiometric TiO₂, N-doped TiO₂, black TiO₂) modified with Au nanoparticles (NPs) 3–6 nm in size. The rate of FA photo-oxidation follows different trends depending on Au loading for stoichiometric and doped Au/TiO₂ materials. In the first case, the only contribution of hot electron transfer produces a volcano-shaped curve of photoreaction rates with increasing the Au loading. When TiO₂ contains intra-bandgap states the photoactivity increases linearly with the Au NPs amount, thanks to the concomitant enhancement produced by hot electron transfer and plasmonic resonant energy transfer (PRET). The role of PRET is supported by Finite-Difference Time-Domain simulations, which show that the increase of both Au NPs inter-distance and of SMSI enhances the probability of charge carrier generation at the Au/TiO₂ interface.

1. Introduction

The optimal exploitation of solar light is crucial for increasing the share of renewable energy in chemical and energy industries.^{1,2} Plasmonic photocatalysis recently gained remarkable attention as an emerging approach to enhance the photocatalytic efficiency of metal oxide semiconductors under visible light irradiation.^{3–15}

Plasmonic photocatalysis mainly makes use of metallic nanoparticles (NPs) which can harvest visible light (*e.g.*, Au, Ag or Cu) due to Localized Surface Plasmon Resonance (LSPR).^{16–18} LSPR occurs when the free electrons of a plasmonic NP interact with the incident radiation, oscillating in resonance and against the restoring force of the positively charged surface nuclei.¹⁹

This results in the generation of highly energetic electrons (hot e⁻) and in the capability of concentrating the electromagnetic field in nanoscale volumes.^{9,18} Plasmonic NPs have extremely large absorption cross section and can therefore capture light more efficiently compared to other optical species generally used in sensitization processes, such as semiconductor quantum dots and organic chromophores.^{17,20}

Furthermore, plasmonic NP-based nanocomposites present some fundamental advantages if compared to semiconductor-based photocatalysts. For instance, LSPR can be tuned from visible to near infrared wavelengths by adjusting size and shape of the plasmonic NPs, as well as the environment in their proximity. In addition, they can promote enhanced charge separation,⁸ intense electric field,²⁰ hot electron generation,^{21,22} local heating effects,^{17,23,24} and increased selectivity toward chemical reactions.^{19,23,24}

Depending on the electronic structure of the adjacent semiconductor, LSPR can either promote hot electron transfer²¹ from plasmonic NPs to the semiconductor conduction band (CB) upon crossing the Schottky barrier junction,²⁵ or result in the Plasmon-induced Resonant Energy Transfer (PRET).^{26–28} This latter is possible only when the LSPR wavelength resonates with the semiconductor band-gap (Scheme 1a).^{16,17,19}

TiO₂ is the archetypical semiconductor for plasmonic photocatalysis since its CB energy is favourably located to assure efficient hot electron transfer, while PRET can be enabled after judicious TiO₂ band-gap engineering.^{19,22,26,27}

Despite a large number of reports on plasmon-driven photocatalysis has already appeared, the majority of them

^a CNR-Istituto di Scienze e Tecnologie Molecolari, Via Golgi 19, 20133 Milan, Italy. Email: v.dalsanto@istm.cnr.it; Fax: +39 02 503 14405; tel: +39 02 503 14428

^b Dipartimento di Chimica, Università degli Studi di Milano, Via Golgi 19, 20133 Milan, Italy. Email: elena.selli@unimi.it; Fax: +39 02 503 14300; tel: +39 02 503 14237.

^c Dipartimento di Scienza e Alte Tecnologie, Università dell'Insubria, Via Valleggio 11, 22100 Como, Italy

^d University of Rome "Tor Vergata", Department of Electronic Engineering, Via del Politecnico 1, 00133 Rome, Italy

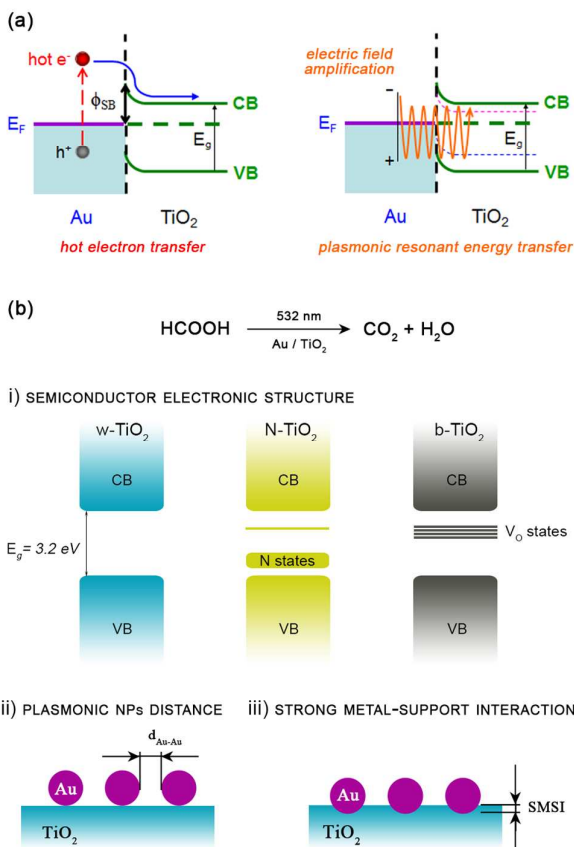
^e Elettra-Sincrotrone Trieste S.C.p.A., S.S. 14 Km 163.5, AREA Science Park - Basovizza, 34149 Trieste, Italy

^f IOM CNR, Laboratorio TASC, S.S. 14 Km 163.5, AREA Science Park - Basovizza, 34149 Trieste, Italy.

[‡] current address: Department of Materials Science WW4-LKO, University of Erlangen-Nuremberg, Martensstrasse 7, 91058 Erlangen, Germany

[†] These authors contributed equally.

Electronic Supplementary Information (ESI) available: characterizations of materials, tables and additional photocatalytic activity plots. See DOI: 10.1039/x0xx00000x



Scheme 1. (a) Plasmonic photocatalysis can proceed through two major mechanisms involving either hot electron transfer (left) or plasmonic resonant energy transfer (right). (b) Schematics of plasmonic FA photooxidation with Au/TiO₂ catalysts, depending on (i) the semiconductor electronic structure, (ii) the Au NPs inter-distance ($d_{\text{Au-Au}}$), (iii) strong metal-support interactions (SMSI).

focus on the proof of concept for single materials featuring precisely designed electronic structure or morphology. There is a lack of understanding on how plasmonic reactions depend on parameters usually considered in catalysis.

Herein, we report on the plasmonic photodegradation of formic acid (FA) performed on Au/TiO₂ photocatalysts, under green LED irradiation. A thorough investigation was performed on the effect induced by (i) the TiO₂ electronic structure, (ii) the Au NPs loading (1–10 wt.%), and (iii) the strong metal-support interaction (SMSI) between Au NPs and the TiO₂ supports (Scheme 1b).

Our aim is to develop a clear correlation between the structural/physical properties and the catalytic activity of widely adopted photocatalysts utilized in powder form.

Specifically, the three investigated TiO₂ supports were stoichiometric TiO₂ (w-TiO₂), N-doped TiO₂ (N-TiO₂) having additional states above the valence band (VB), and black TiO₂ (b-TiO₂) with oxygen vacancy (V_o) electronic states below the CB. Synchrotron x-ray absorption and resonant photoemission spectroscopy allowed to finely determine the electronic

structure of the selected TiO₂ supports. Experimental evidence suggests that different plasmonic mechanisms are involved for w-TiO₂ and doped TiO₂ materials in FA photooxidation: hot electron transfer and PRET, with the latter becoming dominant at high Au loading. The role of PRET is supported by Finite-Difference Time-Domain (FDTD) simulations, which show that the enhancement of both Au NPs vicinity and of SMSI resulted in increased probability of charge carrier generation at the Au/TiO₂ interface and, hence, in better performance in FA plasmonic oxidation.

2. Experimental section

Photocatalysts Synthesis. w- and b-TiO₂ powders were prepared according to a procedure described elsewhere.²⁹ Briefly, the w-TiO₂ sample was obtained by annealing a high surface area TiO₂ commercial powder (BET surface area $\geq 500 \text{ m}^2 \text{ g}^{-1}$) at 773 K for 1 h under continuous O₂ flow; similarly, the highly defective b-TiO₂ was prepared by annealing the same commercial TiO₂ precursor under H₂ stream.²⁹ The N-doped TiO₂ powder (hereafter, N-TiO₂) was synthesized starting from titanium(IV) isopropoxide (TTIP, Aldrich 97%) as Ti precursor. The required amount of a NH₂OH/H₂O solution (N/Ti = 25 mol. %) was added drop-wise to 100 mL of anhydrous ethanol, also containing 10 mL of dissolved TTIP, and it was heated at 30°C under vigorous stirring. After stirring and refluxing for 1 hour, the organic residues were eliminated. Finally, the powder was annealed at 500°C for 4 h under air flow. Elemental analysis evidenced a 0.1 wt.% content of nitrogen into the TiO₂ lattice. The prepared w-, N- and b-TiO₂ supports were surface modified by deposition of Au NPs through the NaBH₄ reduction method.³⁰ The Au-modified powders were labelled as x%Au/w-, b- or N-TiO₂, with x referring to the Au nominal loading (ranging from 1 to 10 wt.%).

Photocatalysts Characterization. XRPD measurements were performed with a Siemens D500 diffractometer operating at 40 kV and 30 mA, at Cu K α radiation source. The XRPD patterns were analysed with the Rietveld method as implemented in the GSAS software suite of programs.^{31,32} The crystallite size was determined by applying the Scherrer equation. The optical properties of the powders were determined by means of a UV-visible spectrophotometer (Thermo Scientific Evolution 600), equipped with a diffuse reflectance accessory Praying-Mantis sampling kit (Harrick Scientific Products, USA). High Resolution Transmission Electron Microscopy (HRTEM) was employed to determine the morphology and size distribution of metallic Au NPs supported on TiO₂, using a Zeiss Libra 200FE instrument. TEM micrographs were taken spanning wide regions of all examined samples in order to provide a truly representative statistical map of the powders. The size distribution of the Au NPs deposited on TiO₂ was calculated by sampling, on average, 400 metallic NPs. X-ray absorption spectroscopy (XAS) and resonant photoemission spectroscopy (RESPES) were recorded at the BACH beamline at the Elettra synchrotron facility in Trieste (Italy). XAS experiments were carried out in total electron yield mode with monochromator resolution set to 0.1 eV, at the Ti L_{2,3}-edge photon energy. RESPES data were

collected by scanning the photon energy from 456 to 470 eV with energy steps of 0.20 eV. The actual Au loading of each photocatalyst sample was determined by ICP-OES (ICAP 6300, Thermo Electron) after microwave digestion of samples in a 3:1 HCl/HNO₃ mixture. The specific surface area (SSA) of Au/TiO₂ samples was determined by Kr physisorption at 77 K, employing a multipoint BET interpolation of the adsorption isotherm (ASAP 2020, Micromeritics). All measurements were repeated twice and the mean value was reported. Around 20 mg samples were outgassed at 473 K for 1 h under high vacuum before carrying out Kr adsorption.

FDTD Simulations. Optical simulations were performed by means of the electromagnetic tool of the Comsol Multiphysics package. In particular the RF module was used, which solves Maxwell's equation using the finite element method (FEM). The full-wave formulation was selected since it permits to solve the total electromagnetic fields including also sources in the model. Since the device was studied at a single frequency (corresponding to the irradiation wavelength adopted for the photoactivity tests, *i.e.*, $\lambda = 532$ nm) the simulation was done with the frequency domain solver. A plane electromagnetic wave is incident at the top of the defined geometry. The incoming plane wave travels in the negative y direction (from the top to the bottom of the structure), with the electric field polarized along both x and z-axis. The input electric field has unitary amplitude (1 V m⁻¹). A perfectly matched layer (PML) domain is placed outside the whole domain and acts as an absorber from the field eventually reflected from the Au NPs and the TiO₂ substrate. Since in the real samples Au NPs have random positions, in simulations we considered a large number of NPs and we did not consider periodic boundary conditions, in order to reproduce a model as accurate as possible. A tetrahedral mesh was used to better fit the Au NPs geometry. See Electronic Supplementary Information (ESI) for parameters used in the simulations. The following formula was applied to calculate the Enhancement Factor (EF):²⁷

$$EF = \frac{\int_{-10 \text{ nm}}^0 dz \int dx dy |E|^2}{\int_{-10 \text{ nm}}^0 dz \int dx dy |E_0|^2}$$

E_0 was the electric field of the incident light, while E the field propagating from the plasmonic Au NPs.

Photocatalytic Activity. FA photodegradation was performed under atmospheric conditions following the procedure described in details elsewhere.^{33,34} A home-built LED array (emitting visible light centred at $\lambda = 532 \pm 20$ nm) was used as irradiation source, kept at a fixed distance from the photoreactor. The incident light intensity, measured within the reactor, was *ca.* 6 mW cm⁻², as checked prior to any photocatalytic run by means of an optical powermeter (ThorLabs, PM 200). The photocatalyst amount and the FA initial concentration were fixed at 0.2 g L⁻¹ and 1.0 × 10⁻³ mol L⁻¹, respectively. The residual amount of formate anions contained in aliquotes withdrawn every hour from the photoreactor was determined by Ion Chromatography.³³ The

pH of the suspensions was always in the 3.5 – 3.9 range. All photocatalytic runs were conducted at 298 K (LED irradiation did not produced any temperature variation for the whole reaction duration) and lasted 5–7 h, depending on the investigated sample, they were repeated at least twice to check their reproducibility.

3. Results and discussion

Characterization of TiO₂ supports

Figure 1a shows the XRPD patterns of the three different TiO₂ supports. The powder crystallized in an oxygen atmosphere (*i.e.*, w-TiO₂) was composed of pure anatase TiO₂, while a mixed phase composition (81 wt.% anatase, 19 wt.% rutile) was determined for b-TiO₂.^{29,35} N-TiO₂ was instead composed of nearly pure anatase, with small amounts of rutile (2 wt.%) (see Figure S1). By applying the Scherrer equation to the [101] anatase reflection, the crystallite size was found to be 16 nm, 22 nm and 23 nm for w-, N- and b-TiO₂, respectively (Table S1). w- and N-TiO₂ presented nanocrystals with well-defined boundaries, while b-TiO₂ had a typical core-shell morphology defined by a 1 nm-thick disordered layer (Figure S2).²⁹

Figure 1b reports the UV-vis absorption spectra of the investigated TiO₂ samples: w-TiO₂ (blue line) and N-TiO₂ (red line) exhibited an absorption threshold at *ca.* 380 nm, with the latter showing an additional shoulder at $\lambda \sim 400$ –550 nm (see inset Figure 1b), typical of nitrogen-doped TiO₂.³³ This indirectly provides evidence for the formation of intra band-gap states in N-TiO₂ related to bulk modification.³⁶ An even more extended modification of the TiO₂ lattice was achieved by H₂ thermal treatment. b-TiO₂ (black line) exhibited a featureless broad band absorption for $\lambda > 400$ nm owing to the extra charges due to oxygen vacancies (V_Os).^{26,29}

The determination of band-gap narrowing and the location and nature of electronic/structural defects allow rationalising possible interactions between TiO₂ and the hot electrons or the enhanced electric field of Au.

N-doping is known to produce defect states above the edge of the TiO₂ VB, with a consequent red shift of the absorption threshold.³⁷ In particular, two different N-species can be formed in the bulk of TiO₂, namely, substitutional N (N_s, which replaces an O atom in the Ti---O---Ti lattice) and interstitial N (N_i, which forms a direct bond with a lattice O atom leading to a π radical NO species). The energy levels of N_s are located \sim 0.1 eV above the VB of TiO₂, while those of N_i are slightly more negative (\sim 0.6 eV).^{37,38} Instead, in the b-TiO₂ sample, we

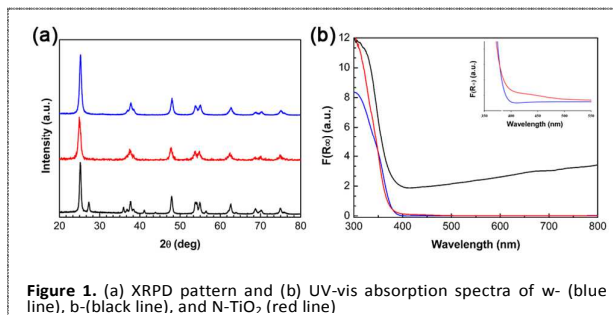


Figure 1. (a) XRPD pattern and (b) UV-vis absorption spectra of w- (blue line), b-(black line), and N-TiO₂ (red line)

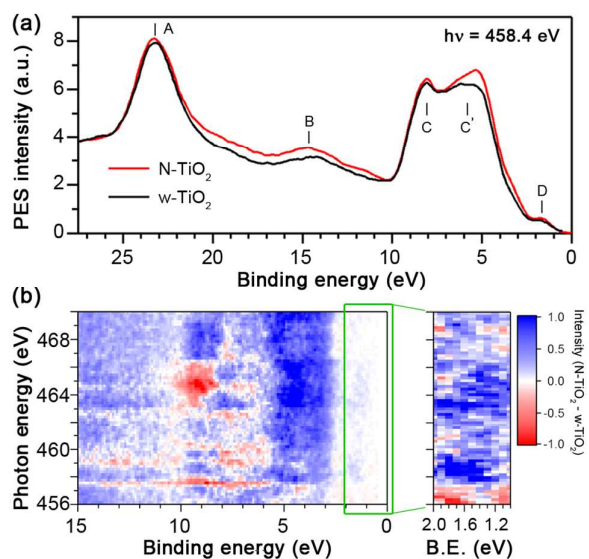


Figure 2. (a) Photoemission spectra collected under resonant conditions (Ti L_{2,3}-edge, $h\nu = 458.4$ eV) for w-TiO₂ (black line) and N-TiO₂ (red line) in the VB region. (b) Difference between RESPES data of N-TiO₂ and w-TiO₂. The plot on the right highlights the increased DOS in the VB region due to N doping. The intensity of the enlargement relative to the 1–2 eV region is enhanced by a factor of 10, compared to the original.

recently reported that the introduction of V_Os induce the formation of intragap energy levels close to the TiO₂ CB,^{26,29} while the surface disorder produces a substantial shift of the VB position.^{29,39}

By means of synchrotron XAS, we investigated the effect of the phase composition and of the introduction of defects on the partial Density of States (DOS) of TiO₂ CB (Figure S2). The line-shape of the Ti L_{2,3}-edge is determined by the 2*p*–3*d* dipole transition. Spin-orbit splitting of the 2*p* orbitals into 2*p*_{3/2} (L₃) and 2*p*_{1/2} (L₂), and crystal field splitting of the 3*d* orbitals into e_g and t_{2g}, generated four absorption peaks for the Ti L-edge.⁴⁰ TiO₂ spectra in Figure S2 are consistent with previous literature reports on the anatase L-edge spectra.^{40,41} Though this result is predictable for w-TiO₂ and N-TiO₂ samples, owing to their pure anatase phase composition, the relatively high content of rutile phase in b-TiO₂ did not influence the XAS line-shape, thus remarking the predominant anatase contribution also in the latter sample. The XAS spectra of w- and N-TiO₂ samples showed similar spectral features in the investigated energy range. Noteworthy, the energy splitting of the t_{2g}–e_g at the L₂-edge was slightly larger in the b-TiO₂ sample than in w- and N-TiO₂ (*i.e.*, 2.0 eV and 1.9 eV, respectively). This may be attributed to possible crystal field changes induced by the incorporation of ~ 5% V_Os in the b-TiO₂ lattice.^{29,42–44}

In the present work, N-TiO₂ had N content as low as 0.1 wt.% and thus the amount of V_O is expected to be extremely low. RESPES was envisaged as a suitable technique to deeply investigate the electronic structure of N-TiO₂. In typical RESPES experiments, the VB photoemission spectra are collected by sweeping the photon energy through an absorption edge.⁴³ Here, we collected seventy VB photoemission spectra across the Ti L_{2,3}-edge to precisely determine both the energy and the

intensity of Ti-related states in the VB region. Figure S5 and S6 report the contour plots of the RESPES data collected on the Ti L-edge for w- and N-TiO₂, respectively. Each line represents a single photoemission spectrum collected at the photon energy reported on the vertical axis. In order to highlight the difference between the VB electronic structure of w- and that of N-doped TiO₂, only the VB photoemission spectra collected under resonance conditions (*i.e.*, at $h\nu = 458.4$ eV) are reported in Figure 2a.^{45,46} Peak A, centred at Binding Energy (BE) = 23.3 eV for both w- and N-TiO₂, was assigned to the O 2s shallow core level. Peak B, which was constant at low photon energy but in both samples shifted to higher values as the photon energy increased above 458 eV, exhibited the so-called Raman-Auger to normal Auger transition. TiO₂ VB is dominated by O 2*p* states, whose photoemission features are located in the 4–8 eV BE region.⁴⁷ However, due to the hybridization between Ti 3*d* and O 2*p* states, a contribution to the VB may arise also from the Ti 3*d* states.^{43,48} Accordingly, the TiO₂ VB of w- and N-TiO₂ samples exhibited the two typical peaks C (BE ~ 8.1 eV) and C' (BE ~ 5.8 eV) which are related to the Ti-O bonding part and non-bonding part of the VB, respectively.^{40,46} Interestingly, the comparison between the two samples highlights that N-TiO₂ exhibited a higher DOS with respect to w-TiO₂, as outlined by the more pronounced C' peak (Figure 2a). In addition, N-doping produced a VB extension toward the Fermi level, which resulted in the typical red-shifted onset in the UV-vis absorption spectra (Figure 1b). The contribution at the top of the VB and at lower BE was ascribed mainly to N states.⁴⁵ At 1 eV < BE < 2 eV, peak D, detected only under resonance condition (*i.e.*, $h\nu = 458.4$ eV), was ascribed to the presence of V_Os, which in turn may generate reduced Ti³⁺ species near the vacancy.^{21,46} Figure 2b shows the differential RESPES considering N-TiO₂ and w-TiO₂ data. The plot remarks the increased DOS in the VB region ascribed to N doping, while the enlargement relative to the 1–2 eV region shows that N-TiO₂ contained also a V_Os concentration higher than that of w-TiO₂. V_Os are reported to give a photoemission peak at around 1.5 eV (see also Figure S7). These defects may arise from water dissociation on V_Os with the consequent formation of Ti 3*d* defect states associated to a Ti–OH bond.³⁷

Morphological and optical properties of Au/TiO₂ photocatalysts

The three TiO₂ supports were modified through the deposition of Au NPs, with the metal nominal amount ranging from 1 up to 10 wt.%. ICP analysis evidenced an increasing Au loading close to the nominal amount for all the investigated powders (Table S2). The deposition of Au on TiO₂ produced metallic NPs well attached to the oxide surface, as shown in the representative Au 5%/w- and b-TiO₂ HRTEM images (Figure 3a and 3b) that highlight the sharp boundaries created at the metal/oxide interface. This morphological feature may ensure high efficiency in hot electron transfer. A similar Au/TiO₂ interface was observed also for N-TiO₂ (Figure S3). The presence of Au NPs led to the appearance of the typical LSPR band for the Au/TiO₂ systems around 530–550 nm (Figure 3c).²³ Au NPs size influences optical properties such as LSPR peak position and absorption intensity.^{34,41}

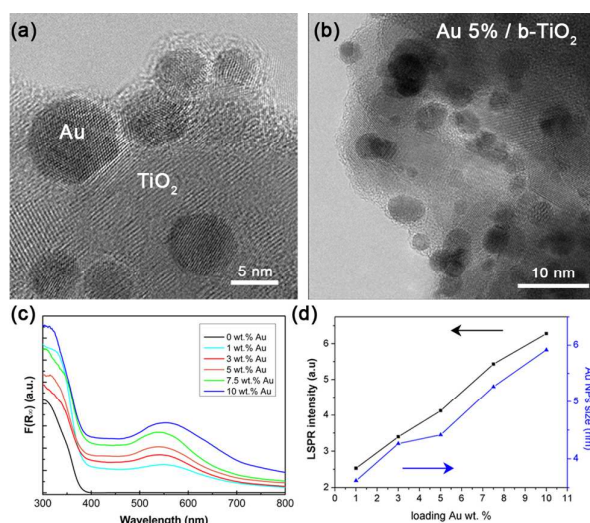


Figure 3. HRTEM image showing the sharp interface formed between Au NPs and (a) w- and (b) b-TiO₂. (c) UV-vis absorption spectra of the x%Au/w-TiO₂ samples. (d) Effect of Au loading on LSPR intensity and Au NPs size for w-TiO₂.

In our materials, LSPR peak positions were not profoundly affected by this morphological parameter since the Au NPs mean size varies within a restrained range (3.2–5.9 nm) (Figure S4). Only a minor red-shift occurs for Au/w-TiO₂ samples as the metal loading increases. By contrast, LSPR bands of Au/N- and Au/b-TiO₂ show no appreciable shift since the metal NPs size is almost constant. The LSPR intensity varies linearly with Au loading for Au/w-TiO₂ (Figure 3d). Conversely, a clear trend could not be found for Au/N- and b-TiO₂ due to the narrow Au NPs size distribution (*i.e.*, around 4.5–5 nm) observed also when varying the Au loading.

FA photocatalytic oxidation

The excitation of Au LSPR can promote photocatalytic reactions on the TiO₂ surface according to (i) hot electron transfer from Au LSPR to the TiO₂ CB (Scheme 1a),^{22,49,50} (ii) Plasmonic-induced Resonant Energy Transfer (PRET),^{19,26,27,51} or (iii) plasmon-induced local heating.^{20,52} In the present study, we purposely used a monochromatic LED source with a 6 mW cm⁻² emission intensity to minimize any thermal effect. We estimated that the temperature increase induced by irradiation on a single Au NP^{20,21} amounted to 3.8×10^{-6} K, which is irrelevant even when considering more Au NPs per TiO₂ crystal (see SI for details).

No FA photodegradation was observed with the three “naked” TiO₂ samples (without Au NPs) both in the dark and under irradiation (Figure S8). Noteworthy, Au NPs deposited on Al₂O₃, a large band-gap semiconductor ($E_g = 8.7$ eV)⁵³ that cannot support neither hot electron injection nor PRET, were not able to promote any photocatalytic reaction.

Under green LED irradiation ($\lambda = 532$ nm), FA photocatalytic degradation occurred according to a zero order rate law, with all the investigated Au/TiO₂ plasmonic composites (see Figure 4a for representative data of 5wt.% Au/TiO₂ samples).³⁴ Thus, the photocatalytic activity of the samples was compared in

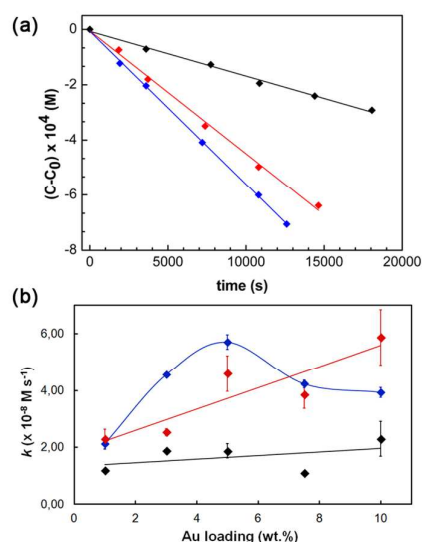


Figure 4. (a) Photocatalytic FA degradation with w-TiO₂ (blue line), N-TiO₂ (red line), and b-TiO₂ (black line) modified with 5 wt.% of Au NPs. (b) Zero order rate constants (k) of FA photodegradation, obtained with the three TiO₂ supports, modified by deposition of different Au NPs amounts (Au/TiO₂ = 1 ÷ 10 wt.%): x%Au/w-TiO₂ (blue line); x%Au/N-TiO₂ (red line); x%Au/b-TiO₂ (black line).

terms of zero order rate constants (k). Figure 4b summarizes the k values of the plasmon-promoted reaction as a function of Au NPs loading for all w-, N-, and b-TiO₂ samples. Quite different photocatalytic activity trends were obtained with increasing the Au amount. Au/w-TiO₂ samples displayed a volcano-shaped activity trend, while Au/N- and b-TiO₂ showed a nearly monotonous increase of the reaction rate, though showing different slope.

Upon optical excitation, each plasmon can decay either radiatively (scattering) or non-radiatively into a hot e^-/h^+ pair. The non-radiative process becomes the dominant decay channel with decreasing the Au NPs size.¹⁷ Besides LSPR excitation, hot electrons may be generated by incident photons having sufficient energy to promote Au interband transition.^{54,55} However, Au interband transitions occur at energies below 520 nm and we suppressed this process by using a 532 nm irradiation source.

Plasmonic hot electron transfer accounted for the photoactivity of the w-TiO₂ samples. In fact, it is generally accepted that the Schottky barrier height formed at the Au/TiO₂ (anatase) interface (Scheme 1a) is approximately 0.9 eV and that hot electrons generated through Au plasmon excitation may raise up to ~ 2 eV above the metal Fermi level (E_F).^{56,57} Thus, a significant fraction of hot electrons can be directly injected into the semiconductor CB (Scheme 1a) and initiate the photocatalytic reaction on the TiO₂ surface.^{21,22,50,58,59}

In the 1–5 wt.% Au loading range, the rate of FA degradation increased with increasing the Au amount, for all the three series, with 5% Au/w-TiO₂ displaying the highest photoactivity throughout (Figure 4b). The absence of defects in the w-TiO₂ support promoted the photocatalytic activity in the 1–5 wt.% Au loading range. The disordered shell of b-TiO₂ might act instead as a physical barrier for hot electrons injection^{26,29} thus

accounting for the lowest efficiency of Au-modified b-TiO₂ samples.

It is noteworthy to point out that PRET did not promote w-TiO₂ photoactivity due to the mismatch between the band-gap of titania ($E_g = 3.2$ eV) and the resonance of the plasmonic electric field (2.3 eV).^{26,27,59} By contrast, the photoactivity of Au/N- and b-TiO₂ samples may arise from both hot electron transfer and PRET. The introduction of intragap defect states makes also the latter mechanism feasible.^{26,27} In the low loading regime (*i.e.*, 1–3 wt. %), Au NPs deposited on the surface of the doped TiO₂ samples were found to be far apart from each other. This can be considered a limiting factor for the enhanced generation of electron-hole pairs in the semiconductor induced by the intense local field (see FDTD simulations section below) and may further account for the relatively lower photoactivity of Au/N- and Au/b-TiO₂ samples. At higher Au content (*i.e.*, 5–10 wt. %), the plasmonic NPs size increased in the Au-modified w-TiO₂ series (Figure S4 and Table S2), and with this also the scattering probability, so that a minor fraction of hot electrons could be injected into the TiO₂ CB.²⁰ Correspondingly, the plasmon-promoted photoactivity of Au/w-TiO₂ samples decreased (Figures 4b, blue curve). On the other hand, in the high loading regime PRET effectively could promote the photoactivity of defective N- and b-TiO₂ (see Scheme 1a),^{26,27} though a contribution of hot electron transfer cannot be ruled out.

Table S2 reports specific surface area values for all Au-modified TiO₂ photocatalysts. SSA is around 80, 20, and 3 m² g⁻¹ for w-TiO₂, N-TiO₂, and b-TiO₂, respectively. SSA values did not change significantly in the whole Au loading range thus producing high Au NPs density. Figure 5a and S9 shows the TEM images of all Au modified N-doped TiO₂ samples. Au NPs appear uniformly deposited onto the TiO₂ surface and their spatial density increased with increasing the Au nominal content. The mean Au inter-particles distance (d_{Au-Au}) on TiO₂, reported for three representative samples (Figure 5b), followed the trend 1 wt.% Au/N-TiO₂ (6.0 ± 0.3 nm) > 5 wt.% Au/N-TiO₂ (5.4 ± 0.4 nm) > 10 wt.% Au/N-TiO₂ (3.4 ± 0.2 nm). We argue that the local fields generated by increasingly closer single plasmonic Au NPs can couple⁶⁰ and provide sufficient energy to enhance the excitation of TiO₂ charge carriers. Notably, the coupling effect is remarkable when the distance between two particles is as small as half of their diameter.⁶¹ This would justify the different photocatalytic trends discussed for b- and N-TiO₂ samples when compared to w-TiO₂ composites. Due to their reduced band-gap, the electric field propagating from the plasmonic surface promotes electrons from the VB to defective states (b-TiO₂) or from N-states to the N-TiO₂ CB. Such electrons are then consumed at the semiconductor surface by the reduction of O₂ (electron acceptor) dissolved in the reaction suspension under aerobic conditions,¹⁰ yielding the superoxide radical anion O₂^{•-}. FA oxidation may thus be induced either by the oxidizing species produced from O₂ reduction, or by holes generated both in the VB and in plasmonic Au.⁴¹

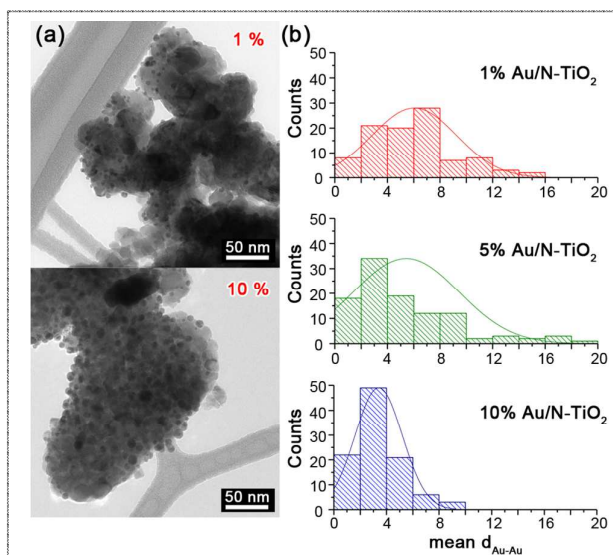


Figure 5. TEM images showing the increased Au NPs density for 1% and 10% Au/N-TiO₂ samples. (b) Mean Au inter-particles distance (d_{Au-Au}) determined from the TEM images of the three representative samples 1, 5 and 10% Au/N-TiO₂.

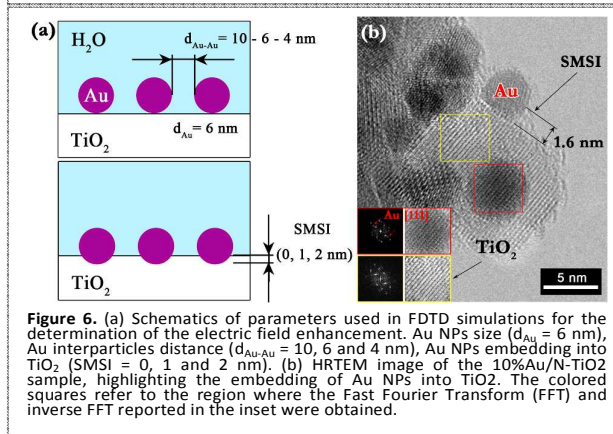


Figure 6. (a) Schematics of parameters used in FDTD simulations for the determination of the electric field enhancement. Au NPs size ($d_{Au} = 6$ nm), Au interparticles distance ($d_{Au-Au} = 10, 6$ and 4 nm), Au NPs embedding into TiO₂ (SMSI = 0, 1 and 2 nm). (b) HRTEM image of the 10% Au/N-TiO₂ sample, highlighting the embedding of Au NPs into TiO₂. The colored squares refer to the region where the Fast Fourier Transform (FFT) and inverse FFT reported in the inset were obtained.

FDTD simulations

In order to validate the role of the PRET mechanism on the photocatalytic activity of the Au-modified doped-TiO₂, we performed Finite-Difference Time-Domain simulations and focused on the effect of the electric field (E) generated by Au plasmons at the Au-TiO₂ interface. The Au-TiO₂ system, in the form of powder dispersed in aqueous suspension, does not consist of isolated TiO₂ NPs, each modified by a single Au NP. It should be rather modelled as TiO₂ submicrometer-sized aggregates (100–200 nm) (see Figure 5a), where several Au NPs are deposited on. Thus, FDTD simulations were performed considering 100–200 nm TiO₂ slides modified by Au NPs with a fixed diameter ($d_{Au} = 6$ nm). The increasing metal loading was simulated by progressively decreasing the Au NPs inter-distance (*i.e.*, $d_{Au-Au} = 10, 6, 4$ nm) (Figure 6a). The experimental inter-distances obtained from TEM images shown in Figure 5b highlight that the proposed model accurately reproduces the Au-modified N- and b-TiO₂ series.

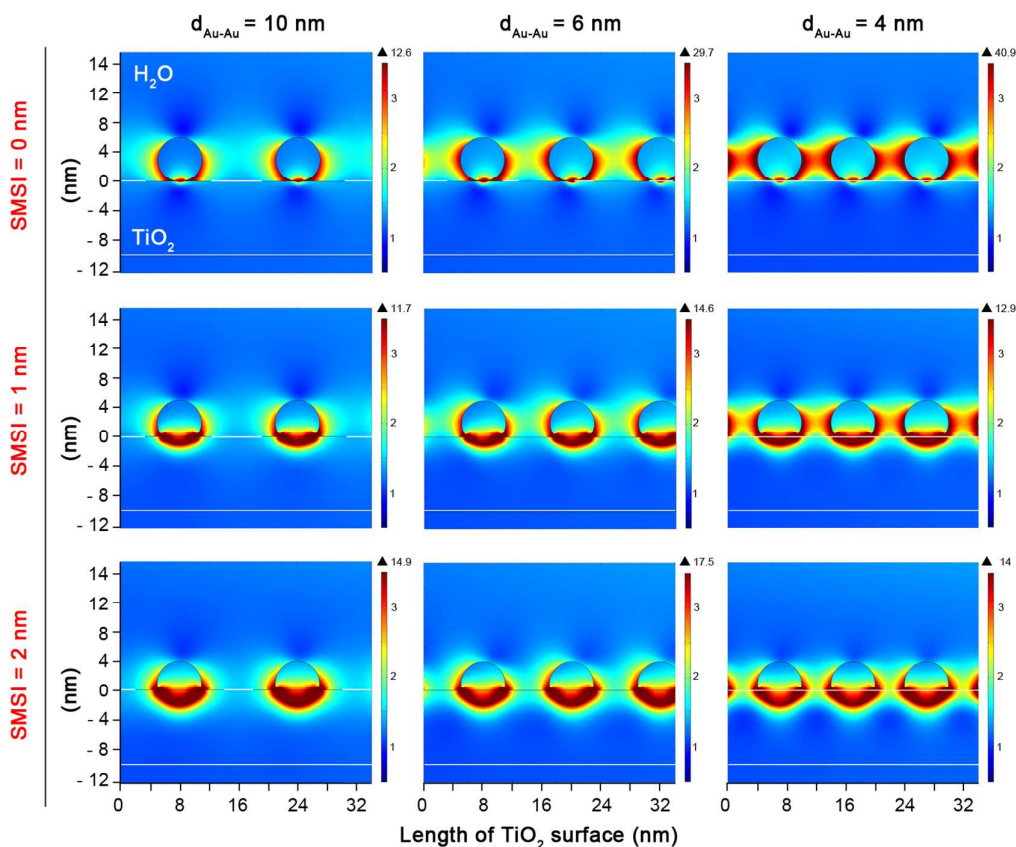


Figure 7. Plasmon-generated electric field intensity, computed by FDTD simulations, as a function of the Au inter-particles distance ($d_{\text{Au-Au}}$). E was calculated along the solid/liquid interface, considering the Au/TiO₂ plasmonic composite immersed in H₂O. In the simulations, Au NPs with a fixed diameter (i.e., $d_{\text{Au}} = 6$ nm) and decreasing inter-distance (i.e., $d_{\text{Au-Au}} = 10, 6, 4$ nm) were considered. In addition, three different geometries were modeled: Au NPs in contact with TiO₂ (SMSI = 0), Au NPs embedded into the TiO₂ slide for 1 (SMSI = 1 nm) and 2 nm (SMSI = 2 nm).

As a novel design parameter for the evaluation of the E enhancement in plasmonic Au/TiO₂ systems, we also took into consideration a well-accepted concept of traditional heterogeneous catalysis, *i.e.* the Strong Metal-Support Interaction (SMSI).⁵⁶ When metal NPs are deposited on oxide supports, the atoms at the metal/oxide interface form real chemical bonds that produce (i) a partial coverage of metal NPs by the oxide support or (ii) an embedding of metal NPs into the surface of the oxide materials (Figure 6). These interactions are particularly strong in Au/TiO₂ composites.^{62,63} For example, from the representative HRTEM image reported in Figure 6b, embedding of Au NPs as deep as ~ 1.6 nm is shown for the 10%Au/N-TiO₂ sample. This morphological feature, which at different extents was observed in all prepared samples, may potentially influence the intensity of the E generated at the Au/TiO₂ interface and, consequently, can affect the plasmon-driven photoactivity.

FDTD simulations were performed taking into account embedding depths = 0, 1 or 2 nm, as SMSI descriptor (Scheme 2). As Au NPs were progressively inserted into the TiO₂ surface, the profile of the E generated by LSPR excitation at the Au/TiO₂ interface (Figure S10). Indeed, instead of a single-hot spot contact (SMSI = 0 nm), two hot spots formed when SMSI

= 1 or 2 nm. Hence, the extent of the TiO₂ region directly adjacent to Au NPs and influenced by the intense E , varied as a function of the Au NPs inclusion.

Figure 7 shows the spatial distribution of the E intensity at the solid/liquid interface, computed by FDTD simulations performed considering Au/TiO₂ immersed in H₂O and by varying $d_{\text{Au-Au}}$ ($d_{\text{Au-Au}} = 10, 6$ and 4 nm). At $d_{\text{Au-Au}} = 10$ nm, when Au NPs laid on the TiO₂ surface (*i.e.*, SMSI = 0 nm, first row), the incident light was concentrated in a single spot at the Au/TiO₂ interface. More deeply in the simulated TiO₂ slide E was only slightly enhanced. When the $d_{\text{Au-Au}}$ was varied from 10 nm to 4 nm (first row, from left to right), the E was around 40 times more intense within adjacent Au NPs. More interestingly, the progressive inclusion of Au NPs into the TiO₂ support led to a pronounced enhancement of the E intensity a few nm under the direct Au/TiO₂ contact. This phenomenon was progressively more evident as $d_{\text{Au-Au}}$ decreased (Figure 7). Indeed, when $d_{\text{Au-Au}} = 4$ nm, the E enhancement extended as deep as 1, 4, and 6 nm into the TiO₂ support for SMSI = 0, 1, and 2 nm, respectively. Therefore, SMSI here reproduced by the partial embedding of Au NPs into the TiO₂ slide introduced a tremendous increase of the semiconductor volume where high intensity plasmon-generated E may enhance the rate of

electron-hole pairs formation. In addition, Figure 7 clearly shows that the $\text{TiO}_2/\text{H}_2\text{O}$ interface (where heterogeneous catalytic reactions typically occur) was also strongly affected by the Au NPs inclusion into the TiO_2 support.

On the basis of the FDTD simulation results, the E Enhancement Factor was also calculated for w- TiO_2 and N- TiO_2 samples.²⁷ The general EF % trend is almost the same for the two catalysts. Since the rate of the incident photon absorption (and, therefore, that of electron-hole pairs generation) is proportional to the square of the plasmon-promoted E ($|E|^2$), we integrated $|E|^2$ over the length of the TiO_2 film used in the simulations (*i.e.*, 100–200 nm) and divided it over the integral of the squared incident E ($|E_0|^2$) (for details see the Experimental Section). Figure 8 shows the EF % calculated for 6 nm-sized Au NPs, by varying the $d_{\text{Au-Au}}$ inter-distance (with $2 \text{ nm} < d_{\text{Au-Au}} < 10 \text{ nm}$, and $\Delta d_{\text{Au-Au}} = 1 \text{ nm}$) and for different Au NPs SMSI (0, 1, and 2 nm). For SMSI = 0 nm, EF was nearly constant, being around 20 % at all the considered $d_{\text{Au-Au}}$ distances for w- TiO_2 and 40 % in the case of N- TiO_2 . Remarkably, for $d_{\text{Au-Au}} = 4 \text{ nm}$ at SMSI = 2 nm an EF % increase of 120 % and 180 % for w- TiO_2 and N- TiO_2 , respectively, was computed (see Figure 8 and Table S4). The maximum EF for SMSI = 2 nm was determined for $d_{\text{Au-Au}} = 4 \text{ nm}$, while the SMSI = 1 nm profile peaked at $d_{\text{Au-Au}} = 3 \text{ nm}$, that is, very close to the experimental $d_{\text{Au-Au}}$ (3.4 nm) observed for 10% Au/N- TiO_2 .

Since in both N- and b- TiO_2 series (*i.e.*, those samples for which PRET mechanism is occurring) SMSI varied in the 1–2 nm range (Figure 6b), the EF trend (Figure 8) can be correlated with the plasmon-promoted photoactivity results (Figures 4b). The monotonic increase in the photocatalytic reaction rate with increasing the Au amount in the b- and N- TiO_2 series was previously explained suggesting a synergistic mechanism involving both hot electron transfer and PRET. In principle, the defect states formed in the electronic structure of TiO_2 upon H_2 -thermal treatment (b- TiO_2) or N-doping (N- TiO_2) may negatively affect the charge carrier diffusion length.^{27,64–66} However, in Au/ TiO_2 plasmonic composites, the Au NPs can couple light effectively from the far-field to the near-field within the minority carrier diffusion length. Consequently, most of the charge carriers created in the semiconductor by the strong plasmon-induced E (*i.e.*, according to PRET mechanism) will reach the TiO_2 surface and contribute to the photocatalytic reaction.²⁷ This most likely accounts for the nearly monotonic increase of the plasmon-induced photoactivity of the Au/doped- TiO_2 samples with PRET becoming the dominant mechanism with respect to hot electron transfer in the high Au loading regime.

Conclusions

The strong interaction between plasmonic nanoparticles and the semiconductor electronic levels strongly influences the mechanism of a plasmon-promoted photocatalytic reaction. Hot electrons can be efficiently transferred to the conduction band of stoichiometric TiO_2 and promote photocatalytic reactions on the semiconductor surface. By contrast, N-doped

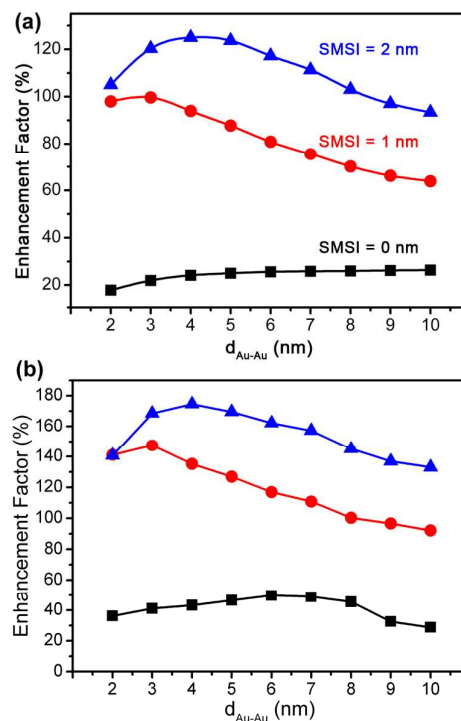


Figure 8. Photocatalytic Enhancement factor of the plasmon-generated electric field for $d_{\text{Au}} = 6 \text{ nm}$ diameter as a function of Au interparticle distance ($d_{\text{Au-Au}}$) at SMSI=0 nm (black line), SMSI=1 nm (red line), SMSI=2 nm (blue line) for w- TiO_2 (a) and N- TiO_2 catalysts (b).

and V_O -rich TiO_2 promote formic acid photodegradation via both hot electron transfer and plasmon resonance energy transfer. This mechanistic aspect was reflected into the different trends of FA degradation rate constants as a function of the Au loading observed for stoichiometric and doped TiO_2 . With increasing the Au NPs loading, TEM images showed that the inter-particles mean distance progressively decreased. FDTD simulation at different inter-particles distance and strong metal-support interaction between Au NPs and TiO_2 support revealed that these parameters are important in the evaluation of the electric field enhancement. Au nanoparticles' coupling was shown to be progressively more efficient for increasingly closer Au NPs. When Au NPs were embedded in the TiO_2 , the electric field propagated a few nanometres below the semiconductor surface ensuring an extended region where charge carriers could be generated. FDTD simulations clearly demonstrated that the maximum enhancement of 180 % for N- TiO_2 can be obtained when $d_{\text{Au-Au}}$ is 3–4 nm, for SMSI = 2 nm. This condition is well represented by the 10wt.% Au loaded N- and b- TiO_2 samples, with the former exhibiting the highest photoactivity at high metal loading. This validated our hypothesis to explain the observed photocatalytic activity trend. In the high Au loading regime PRET become the dominant mechanism with respect to hot electron transfer.

Acknowledgements

VDS, MM and AN acknowledge financial support from Regione Lombardia through the project "TIMES: technology and

materials for the efficient use of solar energy”—Accordo Quadro Regione Lombardia—CNR, and from MIUR through the FIRB project RBF13XUJ9. ES acknowledges financial support from the Cariplo Foundation through the project “Novel photocatalytic materials based on heterojunctions for solar energy conversion”. We acknowledge F. Bondino and E. Magnano of the BACH beamline of the Elettra Synchrotron.

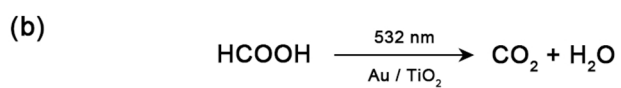
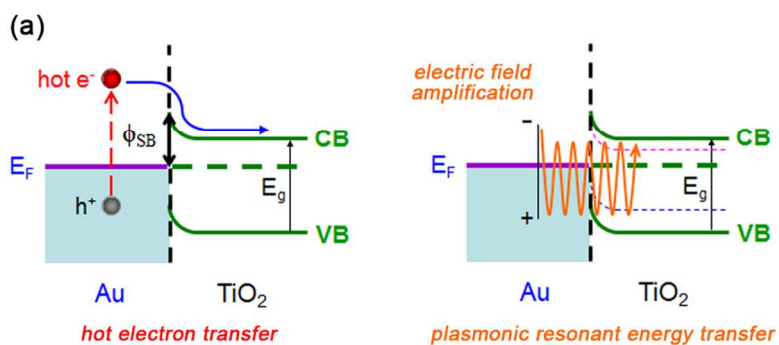
References

- J. Li and N. Wu, *Catal. Sci. Technol.*, 2015, **5**, 1360–1384.
- M. Gao, L. Zhu, W. L. Ong, J. Wang and G. W. Ho, *Catal. Sci. Technol.*, 2015, **5**, 4703–4726.
- S. I. Naya, T. Niwa, T. Kume and H. Tada, *Angew. Chemie - Int. Ed.*, 2014, **53**, 7305–7309.
- X. Huang, Y. Li, Y. Chen, H. Zhou, X. Duan and Y. Huang, *Angew. Chemie - Int. Ed.*, 2013, **52**, 6063–6067.
- Y. Sugano, Y. Shiraishi, D. Tsukamoto, S. Ichikawa, S. Tanaka and T. Hirai, *Angew. Chemie*, 2013, **125**, 5403–5407.
- Y. Tian and T. Tatsuma, *Chem. Commun. (Camb.)*, 2004, 1810–1811.
- R. Long, K. Mao, M. Gong, S. Zhou, J. Hu, M. Zhi, Y. You, S. Bai, J. Jiang, Q. Zhang, X. Wu and Y. Xiong, *Angew. Chemie - Int. Ed.*, 2014, **53**, 3205–3209.
- J. S. DuChene, B. C. Sweeny, A. C. Johnston-Peck, D. Su, E. a. Stach and W. D. Wei, *Angew. Chemie - Int. Ed.*, 2014, **53**, 7887–7891.
- Z. Bian, T. Tachikawa, P. Zhang, M. Fujitsuka and T. Majima, *J. Am. Chem. Soc.*, 2014, **136**, 458–465.
- K. Awazu, M. Fujimaki, C. Rockstuhl, J. Tominaga, H. Murakami, Y. Ohki, N. Yoshida and T. Watanabe, *J. Am. Chem. Soc.*, 2008, **130**, 1676–1680.
- Y. C. Pu, G. Wang, K. Der Chang, Y. Ling, Y. K. Lin, B. C. Fitzmorris, C. M. Liu, X. Lu, Y. Tong, J. Z. Zhang, Y. J. Hsu and Y. Li, *Nano Lett.*, 2013, **13**, 3817–3823.
- A. Primo, T. Marino, A. Corma, R. Molinari and H. García, *J. Am. Chem. Soc.*, 2011, **133**, 6930–6933.
- Q. Xiao, Z. Liu, A. Bo, S. Zavaahir, S. Sarina, S. Bottle, J. D. Riches and H. Zhu, *J. Am. Chem. Soc.*, 2015, **137**, 1956–1966.
- S. Mubeen, J. Lee, D. Liu, G. D. Stucky and M. Moskovits, *Nano Lett.*, 2015, 150216111923008.
- J. Lee, S. Mubeen, X. Ji, G. D. Stucky and M. Moskovits, *Nano Lett.*, 2012, **12**, 5014–5019.
- M. L. Brongersma, N. J. Halas and P. Nordlander, *Nat. Nanotechnol.*, 2015, **10**, 25–34.
- R. Jiang, B. Li, C. Fang and J. Wang, *Adv. Mater.*, 2014, 5274–5309.
- C. Clavero, *Nat. Photonics*, 2014, **8**, 95–103.
- S. Linic, P. Christopher and D. B. Ingram, *Nat. Mater.*, 2011, **10**, 911–921.
- A. O. Govorov, H. Zhang, H. V. Demir and Y. K. Gun'ko, *Nano Today*, 2014, **9**, 85–101.
- L. Amidani, A. Naldoni, M. Malvestuto, M. Marelli, P. Glatzel, V. Dal Santo and F. Boscherini, *Angew. Chemie Int. Ed.*, 2015, **54**, n/a–n/a.
- A. Furube, L. Du, K. Hara, R. Katoh and M. Tachiya, *J. Am. Chem. Soc.*, 2007, **129**, 14852–14853.
- P. Christopher, H. Xin, A. Marimuthu and S. Linic, *Nat. Mater.*, 2012, **11**, 1044–1050.
- P. Christopher, H. Xin and S. Linic, *Nat. Chem.*, 2011, **3**, 467–472.
- M. R. Khan, T. W. Chuan, A. Yousuf, M. N. K. Chowdhury and C. K. Cheng, *Catal. Sci. Technol.*, 2015, **5**, 2522–2531.
- A. Naldoni, F. Fabbri, M. Altomare, M. Marelli, R. Psaro, E. Selli, G. Salviati and V. Dal Santo, *Phys. Chem. Chem. Phys.*, 2015, **17**, 4864–4869.
- Z. Liu, W. Hou, P. Pavaskar, M. Aykol and S. B. Cronin, *Nano Lett.*, 2011, **11**, 1111–1116.
- S. K. Cushing, J. Li, F. Meng, T. R. Senty, S. Suri, M. Zhi, M. Li, A. D. Bristow and N. Wu, *J. Am. Chem. Soc.*, 2012, **134**, 15033–15041.
- A. Naldoni, M. Allieta, S. Santangelo, M. Marelli, F. Fabbri, S. Cappelli, C. L. Bianchi, R. Psaro and V. Dal Santo, *J. Am. Chem. Soc.*, 2012, **134**, 7600–7603.
- A. Naldoni, M. D'Arienzo, M. Altomare, M. Marelli, R. Scotti, F. Morazzoni, E. Selli and V. Dal Santo, *Appl. Catal. B Environ.*, 2013, **130–131**, 239–248.
- N. N. Lobanov and L. Alte de Vega, in *6th European Powder Diffraction Conference*, 1998, pp. P12–16.
- W. Gonschorek and R. Feld, *Zeitschrift. fuer Krist.*, 1982, **161**, 1–5.
- F. Riboni, L. G. Bettini, D. W. Bahnemann and E. Selli, *Catal. Today*, 2013, **209**, 28–34.
- M. V. Dozzi, L. Prati, P. Canton and E. Selli, *Phys. Chem. Chem. Phys.*, 2009, **11**, 7171–7180.
- D. B. Ingram, P. Christopher, J. L. Bauer and S. Linic, *ACS Catal.*, 2011, **1**, 1441–1447.
- C. Di Valentin and G. Pacchioni, *Catal. Today*, 2013, **206**, 12–18.
- C. Di Valentin and G. Pacchioni, *Acc. Chem. Res.*, 2014, **47**, 3233–3241.
- C. Di Valentin, E. Finazzi, G. Pacchioni, A. Selloni, S. Livraghi, M. C. Paganini and E. Giamello, *Chem. Phys.*, 2007, **339**, 44–56.
- X. Chen, L. Liu, P. Y. Yu and S. S. Mao, *Science*, 2011, **331**, 746–750.
- A. G. Thomas, W. R. Flavell, A. K. Mallick, A. R. Kumarasinghe, D. Tsoutsou, N. Khan, C. Chatwin, S. Rayner, G. C. Smith, R. L. Stockbauer, S. Warren, T. K. Johal, S. Patel, D. Holland, A. Taleb and F. Wiame, *Phys. Rev. B*, 2007, **75**, 1–12.
- D. Tsukamoto, Y. Shiraishi, Y. Sugano, S. Ichikawa, S. Tanaka and T. Hirai, *J. Am. Chem. Soc.*, 2012, **134**, 6309–6315.
- X. Chen, P. A. Glans, X. Qiu, S. Dayal, W. D. Jennings, K. E. Smith, C. Burda and J. Guo, *J. Electron Spectros. Relat. Phenomena*, 2008, **162**, 67–73.
- T. Caruso, C. Lenardi, R. G. Agostino, M. Amati, G. Bongiorno, T. Mazza, A. Policicchio, V. Formoso, E. MacCallini, E. Colavita, G. Chiarello, P. Finetti, F. Šutara, T. Skála, P. Piseri, K. C. Prince and P. Milani, *J. Chem. Phys.*, 2008, **128**, 094704.
- A. Braun, K. K. Akurati, G. Fortunato, F. a. Reifler, A. Ritter, A. S. Harvey, A. Vital and T. Graule, *J. Phys. Chem. C*, 2010, **114**, 516–519.
- G. Drera, M. C. Mozziati, P. Galinetto, Y. Diaz-Fernandez, L. Malavasi, F. Bondino, M. Malvestuto and L. Sangaletti, *Appl. Phys. Lett.*, 2010, **97**, 2008–2011.
- G. Drera, L. Sangaletti, F. Bondino, M. Malvestuto, L. Malavasi, Y. Diaz-Fernandez, S. Dash, M. C. Mozziati and P. Galinetto, *J. Phys. Condens. Matter*, 2013, **25**, 075502.

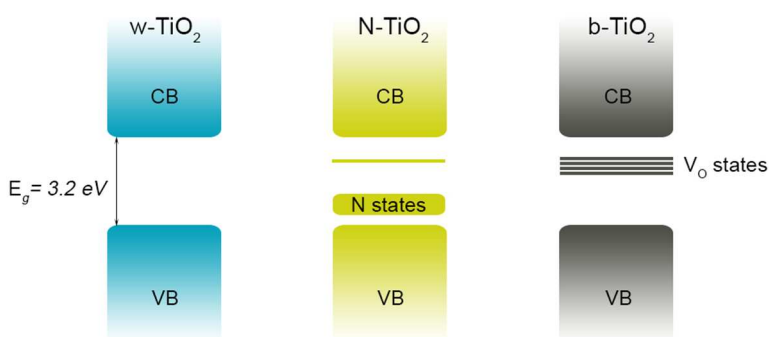
ARTICLE

Catalysis Science and Technology

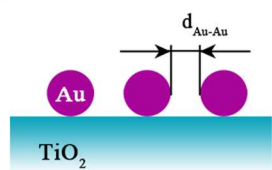
- 47 U. Diebold, *Surf. Sci. Rep.*, 2003, **48**, 53–229.
- 48 A. T. Paxton and L. Thiên-Nga, *Phys. Rev. B*, 1998, **57**, 1579–1584.
- 49 M. J. Kale, T. Avanesian and P. Christopher, *ACS Catal.*, 2014, **4**, 116–128.
- 50 E. W. McFarland and J. Tang, *Nature*, 2003, **421**, 616–618.
- 51 D. B. Ingram and S. Linic, *J. Am. Chem. Soc.*, 2011, **133**, 5202–5205.
- 52 A. O. Govorov, W. Zhang, T. Skeini, H. Richardson, J. Lee and N. a. Kotov, *Nanoscale Res. Lett.*, 2006, **1**, 84–90.
- 53 M. Bäumer and H. J. Freund, *Prog. Surf. Sci.*, 1999, **61**, 127–198.
- 54 L. Liu, P. Li, B. Adisak, S. Ouyang, N. Umezawa, J. Ye, R. Kodiyath, T. Tanabe, G. V. Ramesh, S. Ueda and H. Abe, *J. Mater. Chem. A*, 2014, 9875–9882.
- 55 J. B. Priebe, M. Karnahl, H. Junge, M. Beller, D. Hollmann and A. Brückner, *Angew. Chemie - Int. Ed.*, 2013, **52**, 11420–11424.
- 56 A. Manjavacas, J. G. Liu, V. Kulkarni and P. Nordlander, *ACS Nano*, 2014, 7630–7638.
- 57 R. Sundararaman, P. Narang, A. S. Jermyn, W. a. Goddard III and H. a. Atwater, *Nat. Commun.*, 2014, **5**, 5788.
- 58 R. Long and O. V. Prezhdo, *J. Am. Chem. Soc.*, 2014, **136**, 4343–4354.
- 59 W. Hou and S. B. Cronin, *Adv. Funct. Mater.*, 2013, **23**, 1612–1619.
- 60 N. J. Halas, S. Lal, W. S. Chang, S. Link and P. Nordlander, *Chem. Rev.*, 2011, **111**, 3913–3961.
- 61 U. Cataldi, R. Caputo, Y. Kurylyak, G. Klein, M. Chekini, C. Umeton and T. Buerger, *J. Mater. Chem. C*, 2014, 7927–7933.
- 62 X. Y. Liu, A. Wang, T. Zhang and C. Y. Mou, *Nano Today*, 2013, **8**, 403–416.
- 63 U. Diebold, *Appl. Phys. A Mater. Sci. Process.*, 2003, **76**, 681–687.
- 64 A. C. Arango, L. R. Johnson, V. N. Bliznyuk, Z. Schlesinger, S. a Carter and H.-H. Hörhold, *Adv. Mater.*, 2000, **12**, 1689–1692.
- 65 T. J. Savenije, J. M. Warman and A. Goossens, *Chem. Phys. Lett.*, 1998, **287**, 148–153.
- 66 W. H. Leng, P. R. F. Barnes, M. Juozapavicius, B. C. O'Regan and J. R. Durrant, *J. Phys. Chem. Lett.*, 2010, **1**, 967–972.



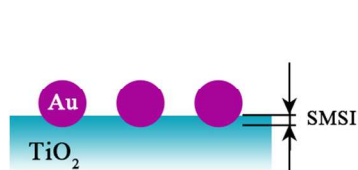
i) SEMICONDUCTOR ELECTRONIC STRUCTURE



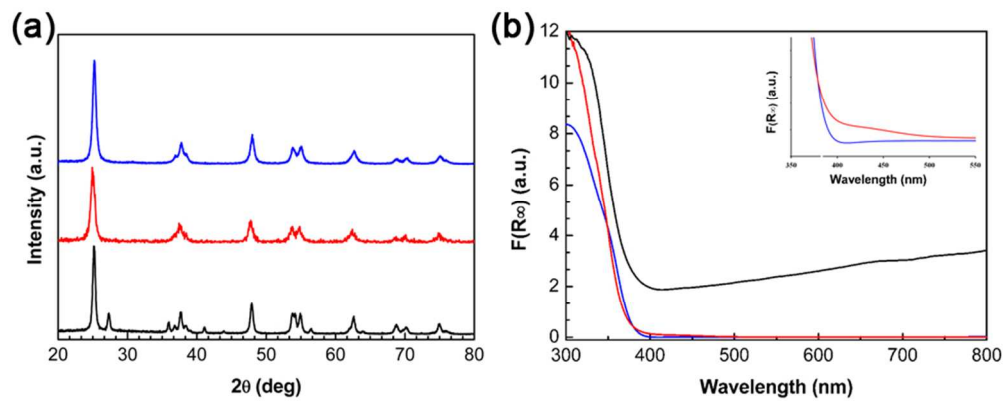
ii) PLASMONIC NPs DISTANCE



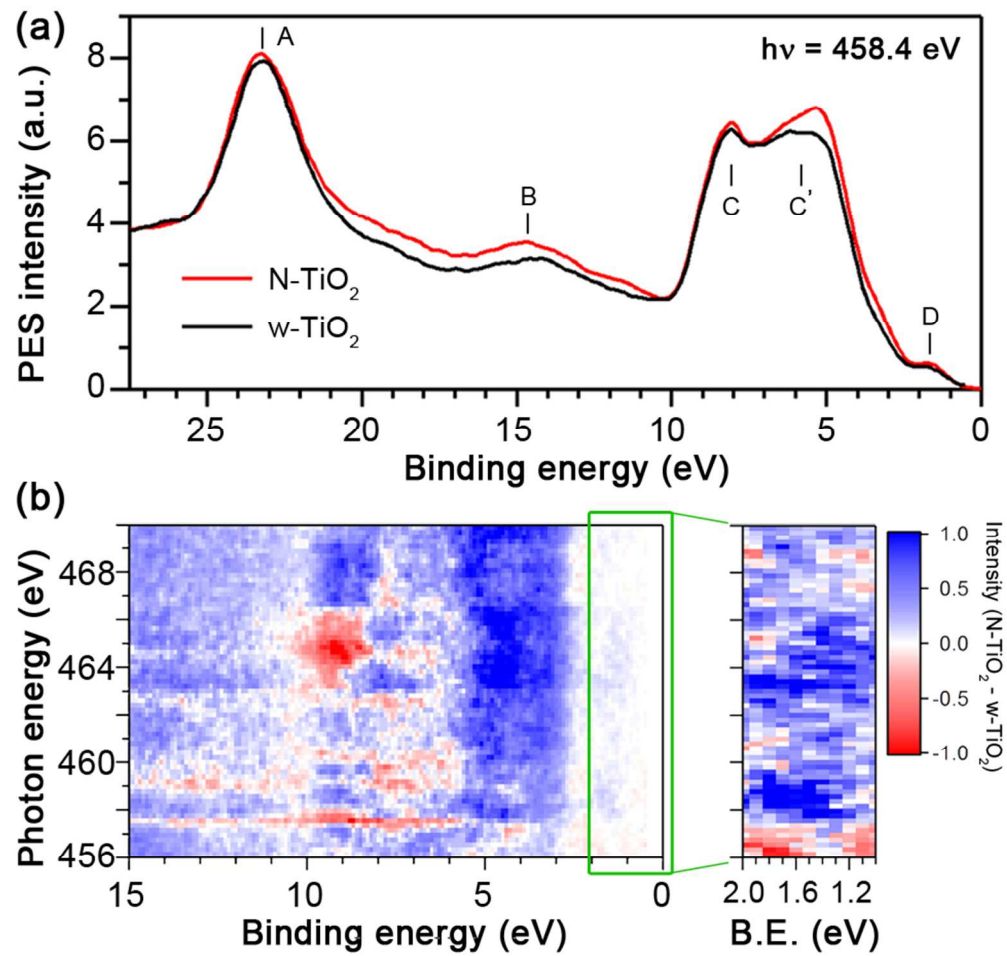
iii) STRONG METAL-SUPPORT INTERACTION



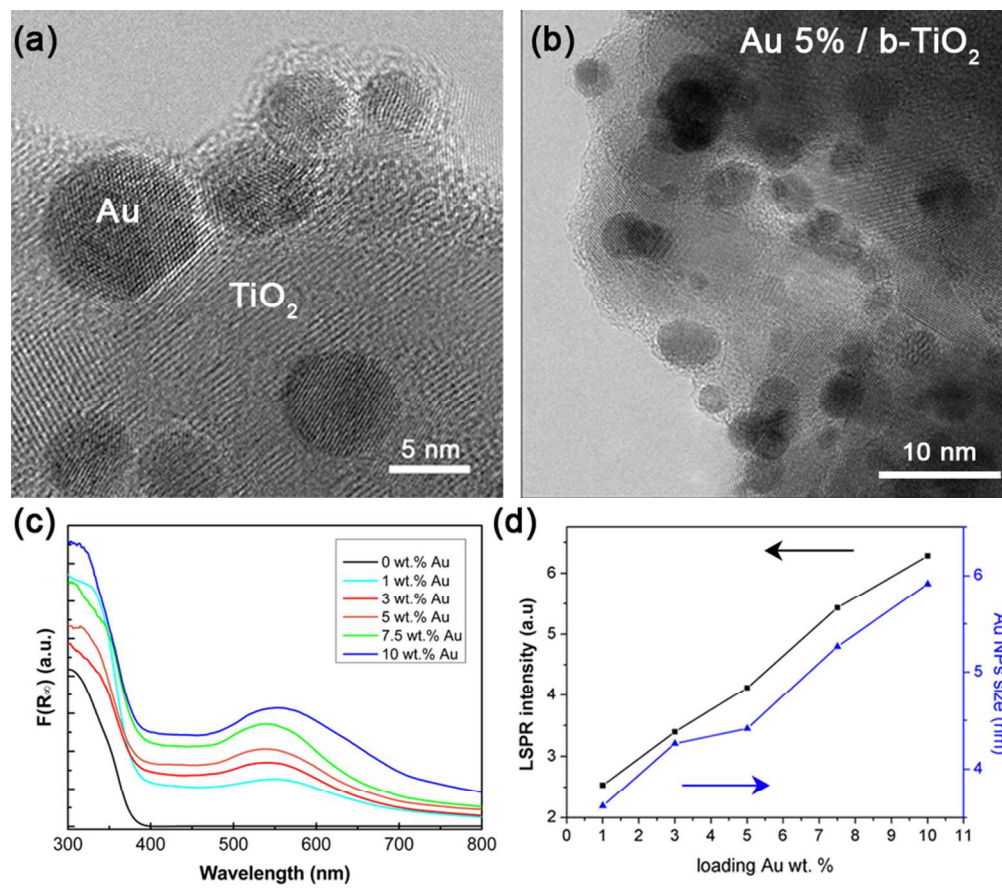
82x125mm (300 x 300 DPI)



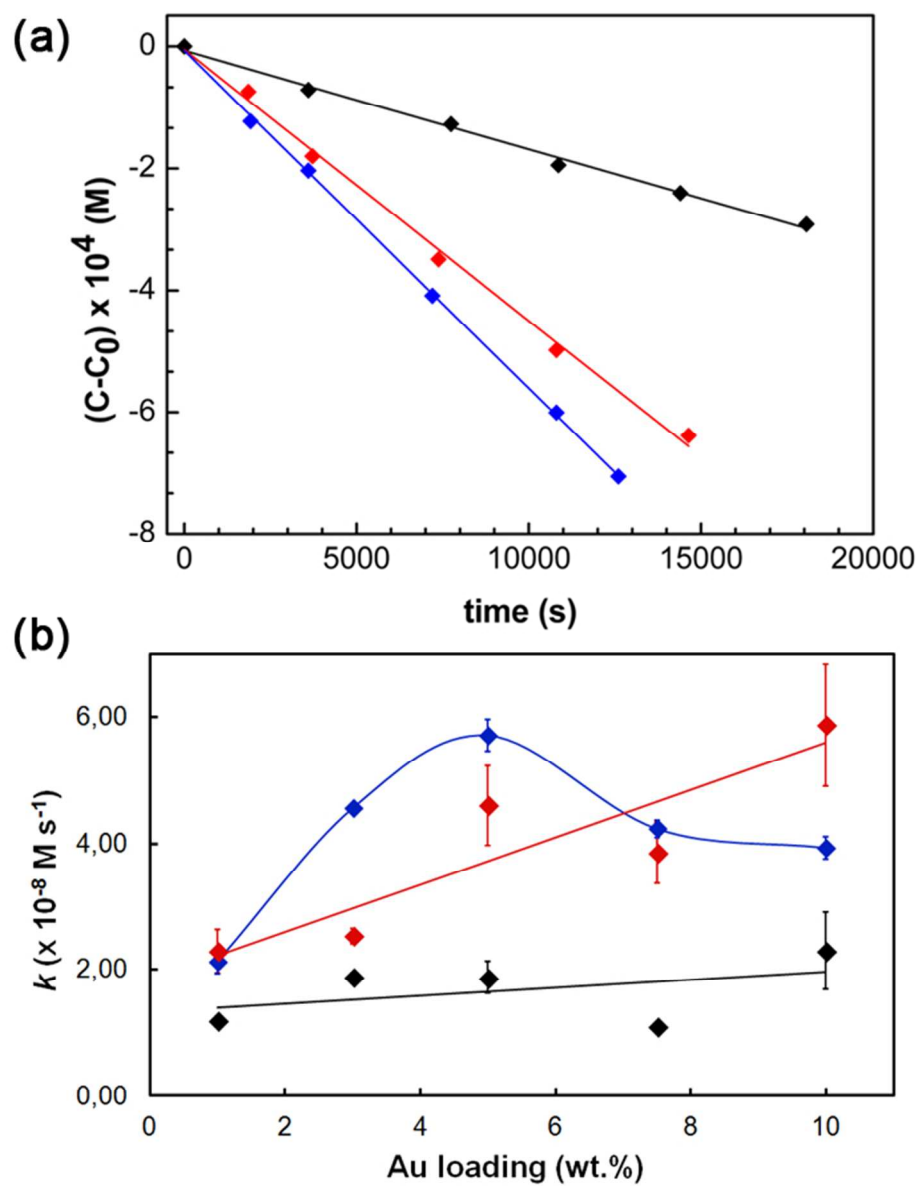
82x33mm (300 x 300 DPI)



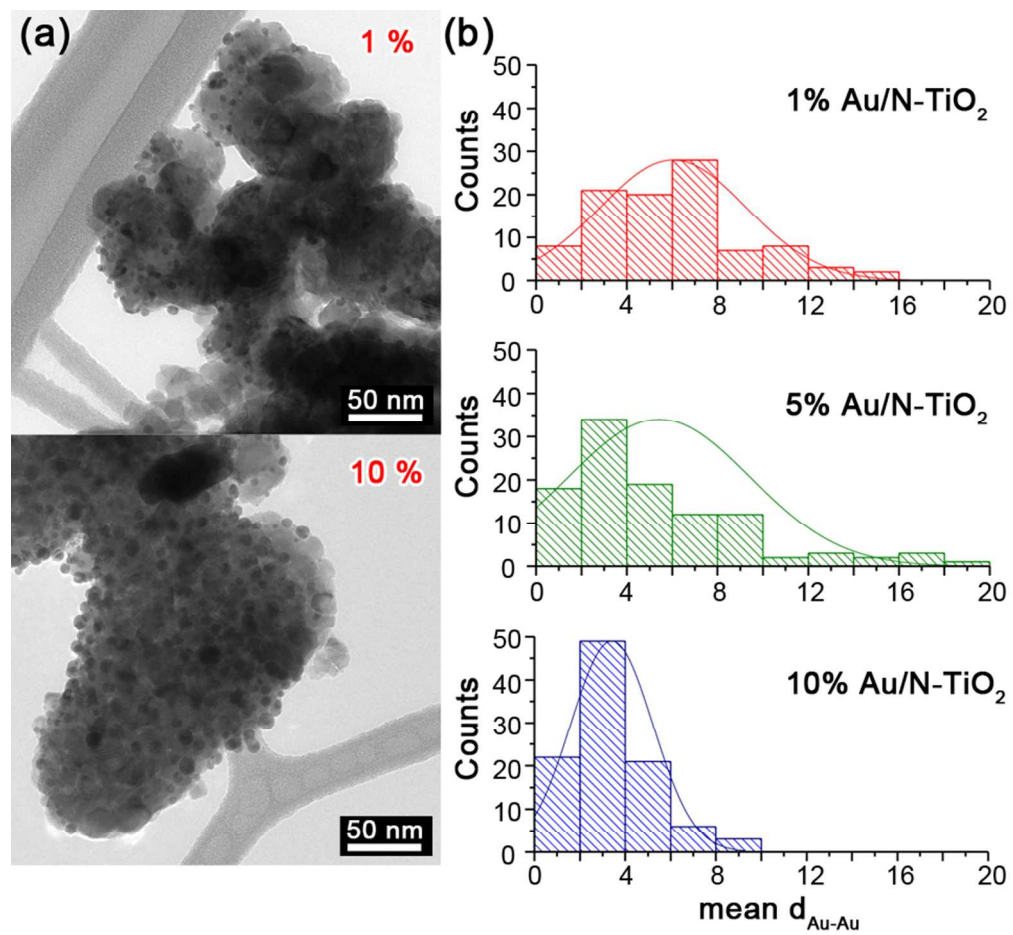
82x79mm (300 x 300 DPI)



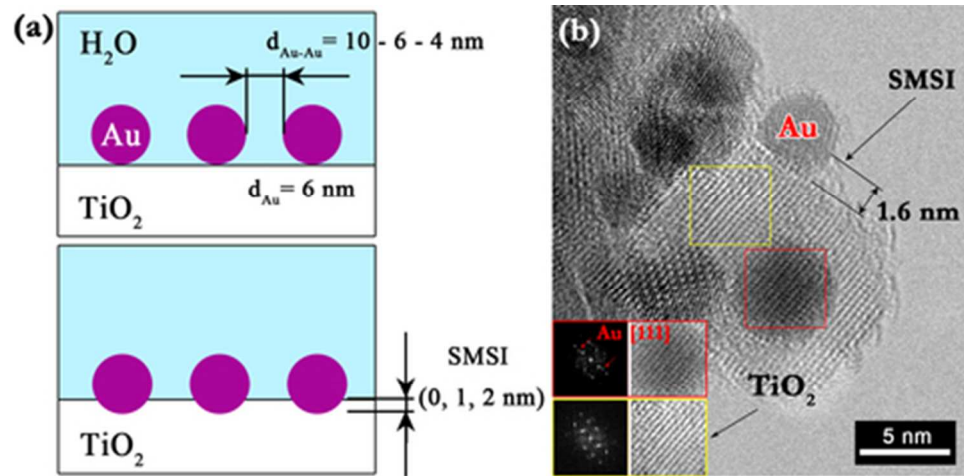
82x72mm (300 x 300 DPI)



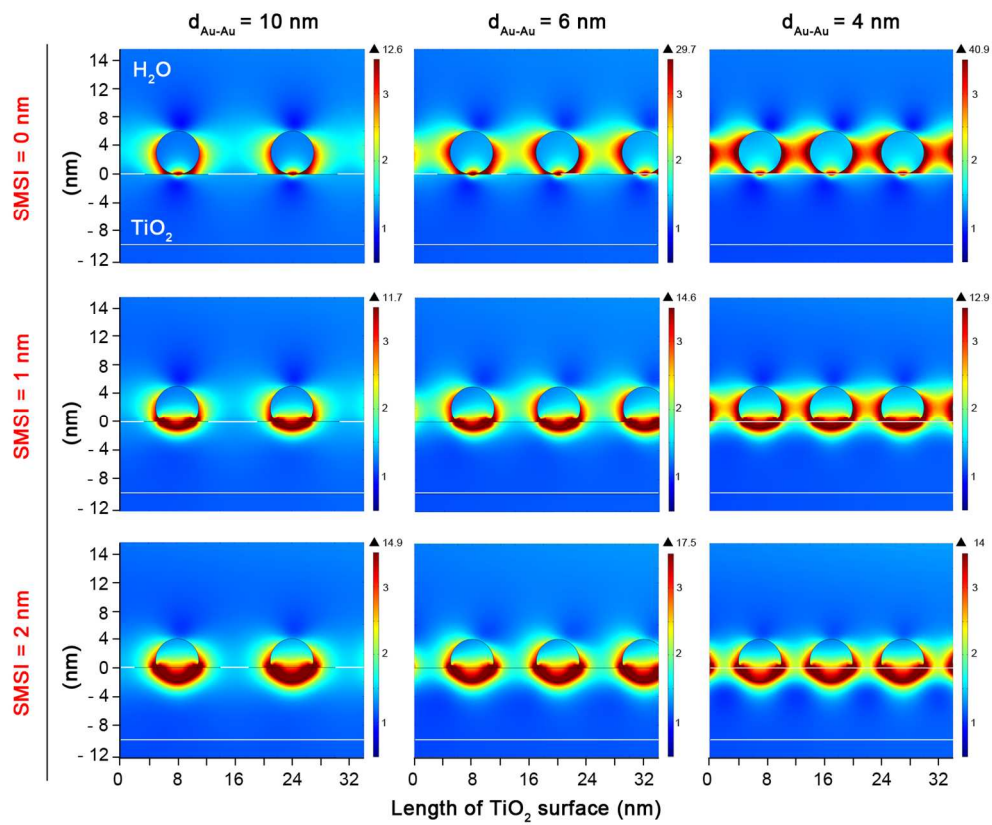
60x76mm (300 x 300 DPI)



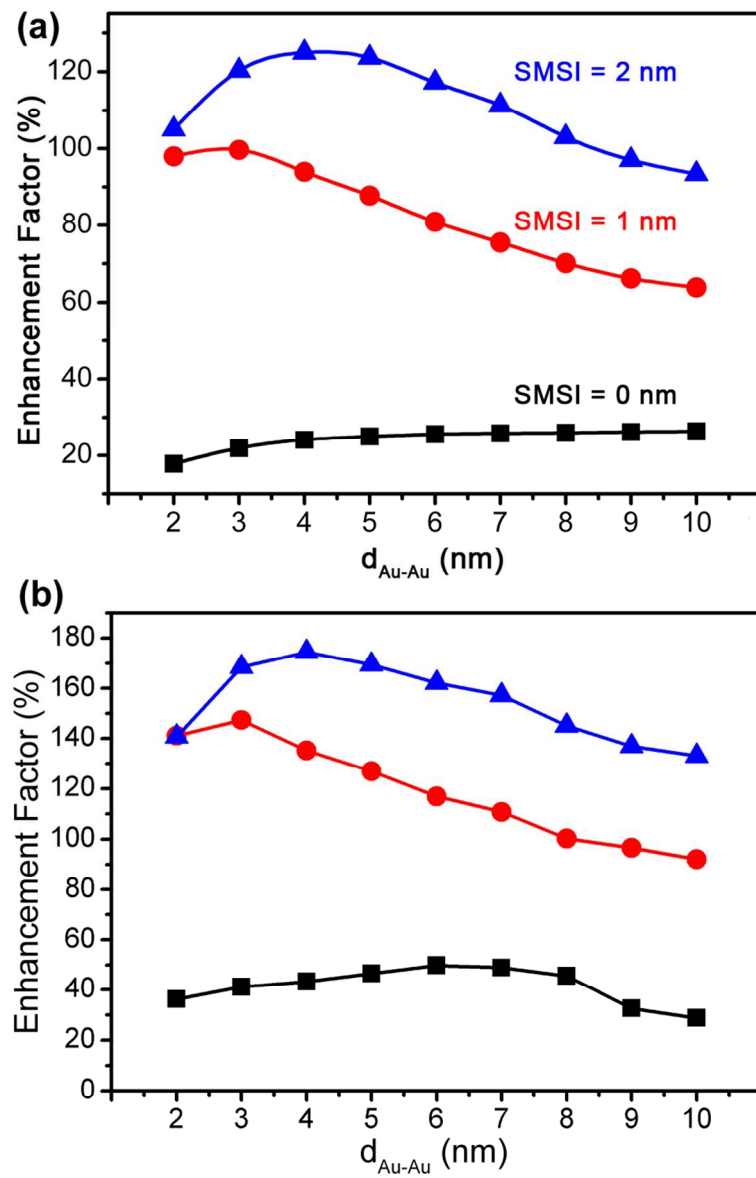
81x74mm (300 x 300 DPI)



40x19mm (300 x 300 DPI)



138x114mm (300 x 300 DPI)

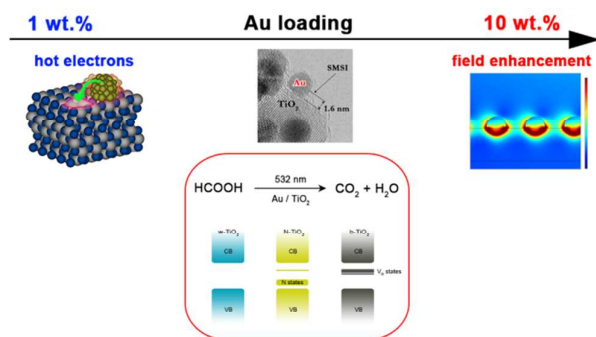


102x128mm (300 x 300 DPI)

Influence of the TiO₂ Electronic Structure and of Strong Metal-Support Interaction on Plasmonic Au Photocatalytic Oxidation

Alberto Naldoni, Francesca Riboni, Marcello Marelli, Filippo Bossola, Giacomo Ulisse, Aldo Di Carlo, Igor Piš, Silvia Nappini, Marco Malvestuto, Maria Vittoria Dozzi, Rinaldo Psaro, Elena Selli and Vladimiro Dal Santo.

Graphical and textual abstract



Structural parameters of plasmonic Au nanoparticles and the semiconductor electronic levels strongly influence the mechanism of a plasmon-promoted photocatalytic oxidations occurring by hot electron transfer and plasmon resonance energy transfer.

Supporting Information for

Influence of the TiO₂ Electronic Structure and of Strong Metal-Support Interaction on Plasmonic Au Photocatalytic Oxidations

A. Naldoni,^a F. Riboni,^{b,*} M. Marelli,^a F. Bossola,^c G. Ulisse,^d A. di Carlo,^d I. Pfs,^{#,f} S. Nappini,^f M. Malvestuto,^e M. V. Dozzi,^b R. Psaro,^a E. Selli,^{*,b} and V. Dal Santo.^{*,a}

^a CNR-Istituto di Scienze e Tecnologie Molecolari, Via Golgi 19, 20133 Milan, Italy

^b Dipartimento di Chimica, Università degli Studi di Milano, Via Golgi 19, 20133 Milan, Italy.

^c Dipartimento di Scienza e Alte Tecnologie, Università dell'Insubria, 22100 Como, Italy

^d University of Rome "Tor Vergata", Department of Electronic Engineering, Via del Politecnico 1, 00133 Rome, Italy

^e Elettra-Sincrotrone Trieste S.C.p.A., S.S. 14 Km 163.5, AREA Science Park - Basovizza, 34149 Trieste, Italy

^f IOM CNR, Laboratorio TASC, S.S. 14 Km 163.5, AREA Science Park – Basovizza, 34149 Trieste, Italy

^{*} *current address*: Department of Materials Science WW4-LKO, University of Erlangen-Nuremberg, Martenstrasse 7, 91058, Erlangen, Germany

Index

Figures	2
Tables	8
Evaluation of heat generated by the Au LSPR excitation	10

Figures

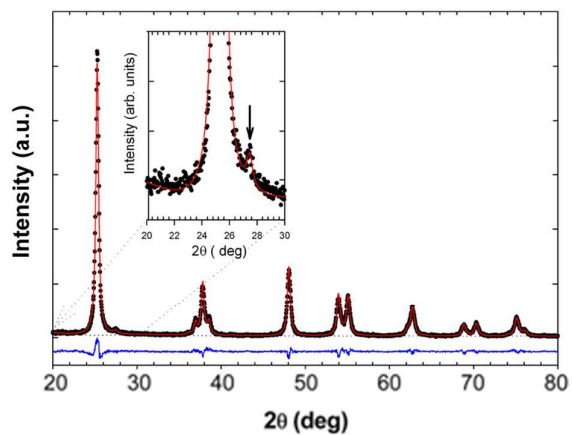


Figure S1. XRPD pattern of N-TiO₂ acquired for long time; the inset represents the zoom of the 2 θ -region where the rutile contribution is clearly visible (peak indicated by the arrow).

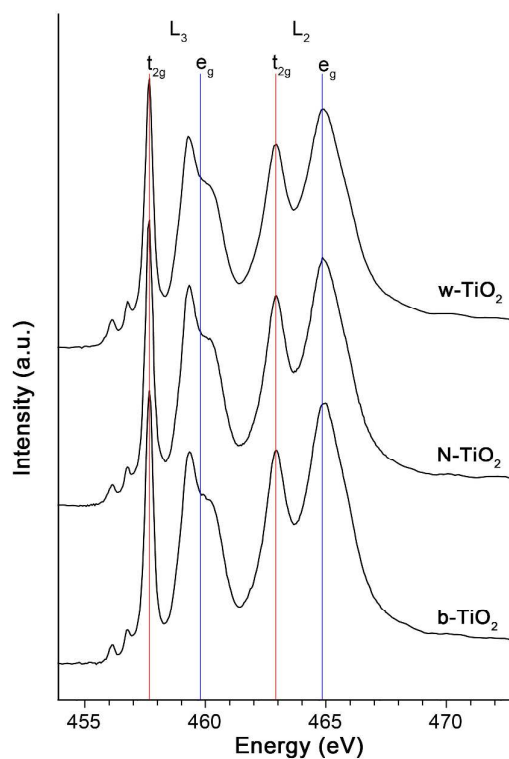


Figure S2. XAS spectra at the Ti L_{2,3} edge of w-TiO₂, N-TiO₂ and b-TiO₂.

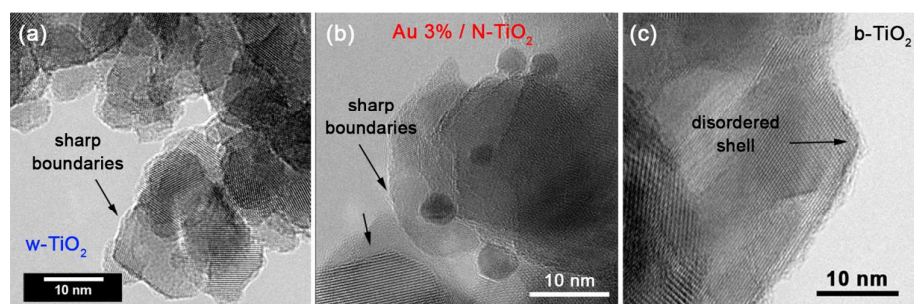


Figure S3. HRTEM micrograph showing the nanocrystal boundary features for (a) w-TiO₂, (b) N-TiO₂, and (c) b-TiO₂. We report representative TEM images that show the Au/TiO₂ interface formed after the Au NPs deposition for Au 3%/N-TiO₂.

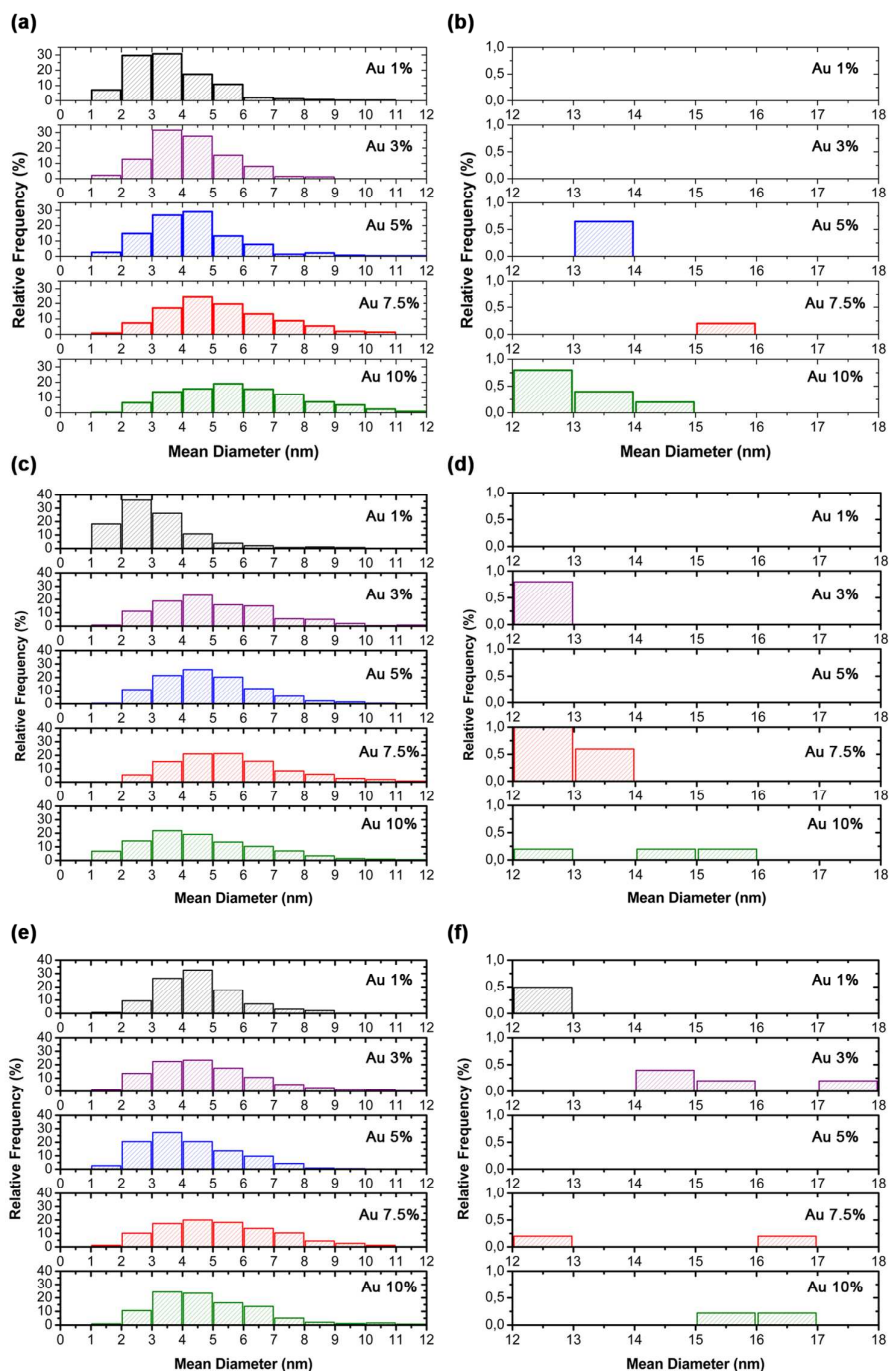


Figure S4. Size distribution obtained from the analysis of TEM images of gold nanoparticles deposited on (a,b) w-TiO₂, (c,d) b-TiO₂, (e,f) N-TiO₂. The size distribution was divided into two dimensional regimes: (a,c,e) represent the 1-12 nm region, while (b,d,f) show the 12-18 nm range for the Au modified w-, b- and N-TiO₂ series.

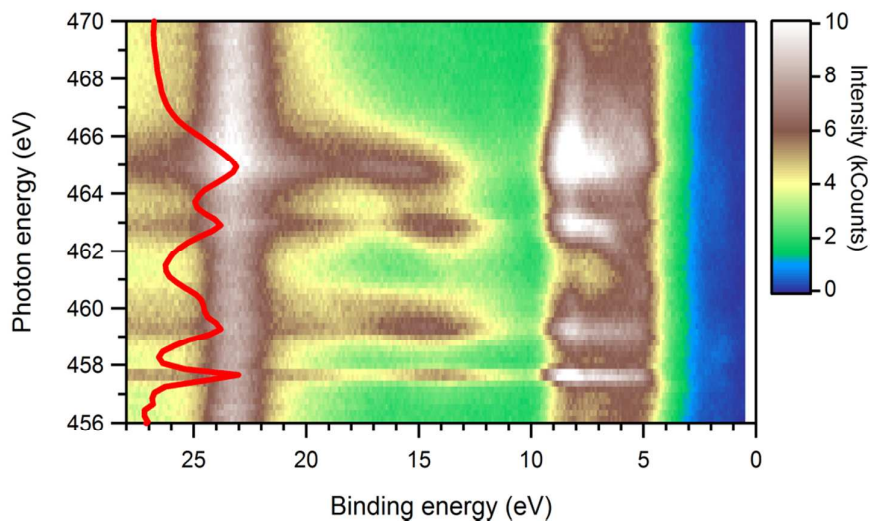


Figure S5. Contour plot of the normalized RESPEC data, along with the Ti $2p-3d$ X-ray absorption spectrum (left axis) for w-TiO₂.

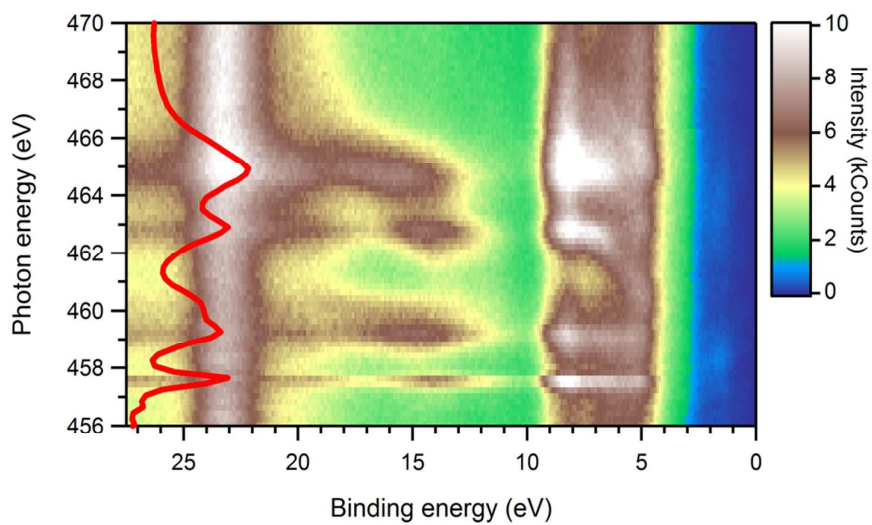


Figure S6. Contour plot of the normalized RESPEC data, along with the Ti $2p-3d$ X-ray absorption spectrum (left axis) for N-TiO₂.

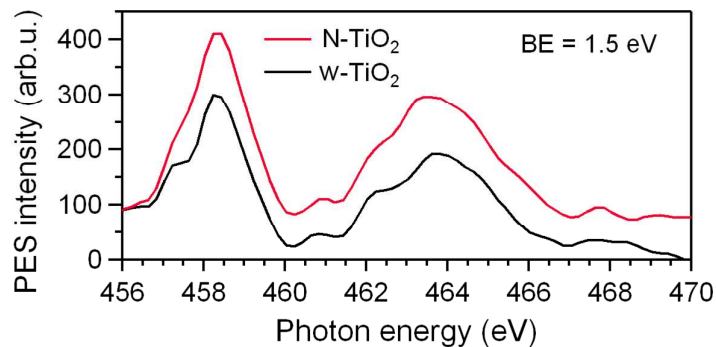


Figure S7. Photoemission spectra (PES) at the maximum of intragap states levels (Binding Energy = 1.5 eV) for w-TiO₂ (black curve) and N-TiO₂ (red curve).

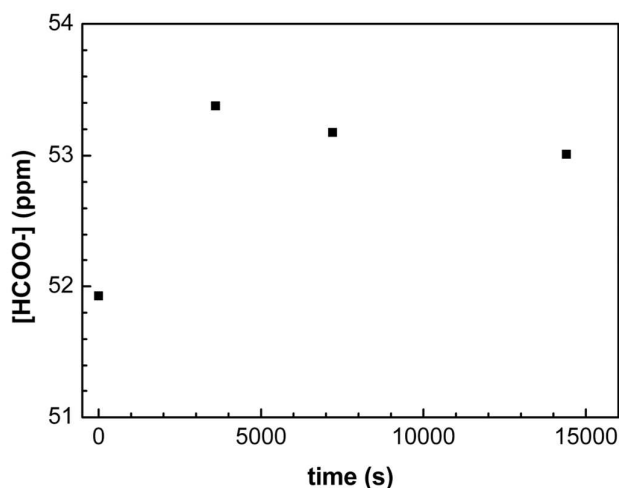


Figure S8. Photocatalytic run of FA degradation performed with bare N-TiO₂.

All the unmodified titania samples (*i.e.*, w-, N- and b-TiO₂ with no Au NPs) exhibited no photoactivity toward FA oxidation (see the representative results for N-TiO₂ in Figure S9(a)), owing to the relatively large band gap of TiO₂ which, notoriously, cannot be excited with visible light ($E_g = ca. 3.2$ eV and $\lambda_{edge} = ca. 380$ nm). These results were a preliminary confirmation that FA photodegradation under green LED irradiation ($\lambda = 532$ nm) is promoted by a mechanism activated by the LSPR of Au NPs.

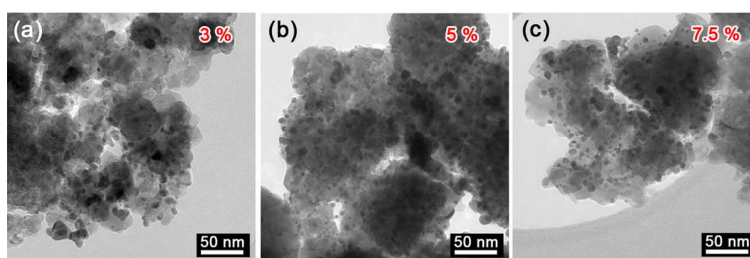


Figure S9. TEM images showing the increased Au NPs density from 3% to 7.5 % Au/N-TiO₂ samples.

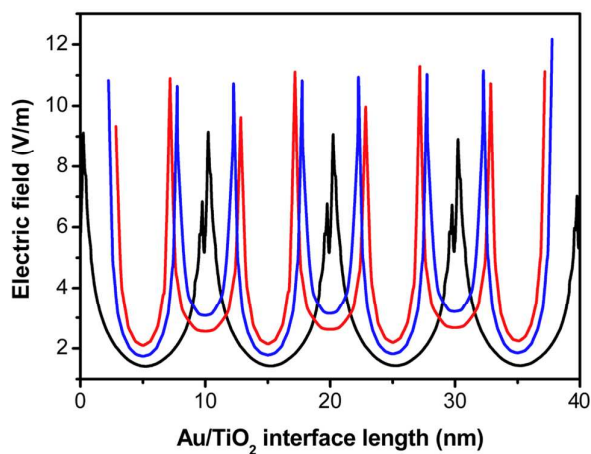


Figure S10. Electric field generated by Au nanoparticles LSPR on the TiO₂ surface. The electric field is strongly enhanced in the point where Au NPs are in contact with TiO₂. In particular, when SMSI = 0 nm (black line), one hot spot forms at the Au/TiO₂ contact point; differently, when SMSI = 1 (red line) and 2 nm (blue line) the profile lines present two hot spots, corresponding to the two-contact Au/TiO₂ interface.

Tables

Table S1. Phase composition (A = anatase, R = rutile) and anatase nanoparticle dimensions, d_A , obtained from XRD analysis.

	Phase composition (wt.%)	d_A (nm)
w-TiO ₂	100 A	16
N-TiO ₂	98 A / 2 R	22
b-TiO ₂	81 A / 19 R	23

Table S2. Real gold content (wt.%) of all investigated photocatalysts, as determined through ICP-OES, Au nanoparticles mean diameter, d_{Au} , obtained from HRTEM analysis, and specific surface area (SSA) for all investigated samples.

Au (wt.%)	w-TiO ₂			N-TiO ₂			b-TiO ₂		
	ICP (wt.%)	$d_{Au} \pm SE$ (nm)	SSA (m ² g ⁻¹)	ICP (wt.%)	$d_{Au} \pm SE$ (nm)	SSA (m ² g ⁻¹)	ICP (wt.%)	$d_{Au} \pm SE$ (nm)	SSA (m ² g ⁻¹)
1	0.70	3.6±0.07	79	0.76	3.2±0.07	21	0.83	4.6±0.07	3.2
3	2.31	4.3±0.06	69	2.69	5.2±0.09	21	2.89	4.9±0.13	4.5
5	4.00	4.4±0.10	79	4.44	4.8±0.07	18	4.48	4.2±0.07	3.3
7.5	6.24	5.3±0.08	65	6.92	5.7±0.09	19	8.66	5.3±0.09	1.2
10	8.90	5.9±0.10	81	8.69	4.7±0.09	16	9.32	4.9±0.10	3.0

Table S3. Refractive index (n) and extinction coefficient (k) values of the materials simulated by means of the Finite Difference Time Domain method. (data taken from: P.-G.Wu, C.-H. Ma, J. K. Shang, Appl. Phys. A 2005, 81, 1411–1417)

Material	n	k
w-TiO ₂	2.5586	4.04e-4
N-TiO ₂	2.400	4.04e-4
H ₂ O	1.334	1.32e-9
Au nanoparticle	0.432	2.437

Table S4. Enhancement Factor (EF %) of the electric field calculated simulating 6 nm-sized Au NPs, with interparticles distance $2 \text{ nm} < d_{\text{Au-Au}} < 10 \text{ nm}$ ($\Delta d_{\text{Au-Au}} = 1 \text{ nm}$) and different extents of metal nanoparticles embedding in the w-TiO₂ and N-TiO₂ supports (*i.e.*, SMSI = 0, 1 and 2 nm). A graphical representation of the data is provided in Figure 8.

$d_{\text{Au-Au}}$ (nm)	Enhancement Factor (EF %)					
	w-TiO ₂			N-TiO ₂		
	SMSI = 0 nm	SMSI = 1 nm	SMSI = 2 nm	SMSI = 0 nm	SMSI = 1 nm	SMSI = 2 nm
2	17.82	97.95	104.98	36,32	141,22	140,73
3	21.95	99.61	120.30	41,11	147,36	168,37
4	24.12	93.95	124.95	43,25	135,30	174,52
5	24.96	87.71	123.63	46,46	126,96	169,41
6	25.57	80.84	117.22	49,77	116,91	162,12
7	25.78	75.51	111.31	48,79	110,79	157,14
8	25.95	70.14	102.99	45,45	100,36	145,04
9	26.16	66.21	97.00	32,65	96,65	136,90
10	26.35	63.89	93.38	28,76	92,14	133,06

Evaluation of the heat generated by Au SPR excitation

Irradiation at the SPR of Au can induce a temperature increase at the surface of the metal NPs, due to strong light absorption; this can even lead to a temperature increase extended to the whole sample supporting the NPs. With continuous LED excitation, energy is uniformly absorbed over time and the temperature increase at the NPs surface can be evaluated considering the heat transfer across the surface of a sphere when a source of constant heat is acting^{1,2}

$$\Delta T = \frac{q_{NP}}{4\pi k_0 R_{NP}}$$

where q_{NP} is the heat generation rate, k_0 is the thermal conductivity of the matrix around the NP and R_{NP} is the NP radius.

To evaluate q_{NP} we started from the absorption cross section σ_{abs} of Au NPs multiplied by the incident LED fluence, I_0 , and considered the borderline case – that is that all the absorbed power is converted into heat. Typical values of σ_{abs} for 5 nm Au NPs in water are in the 10^{-13} - 10^{-14} cm² range.³ During the experiment a continuous fluence of *ca.* 6 mW/cm² was provided, which gives a maximum absorbed power of 10^{-12} W per NP. With these values and considering the thermal conductivity of TiO₂ (5-12 W K⁻¹ m⁻¹) a maximum temperature increase of 6.4 μK per NP is found.

This temperature increase at the surface of each Au NP is not sufficient to induce a relevant heating of TiO₂ and therefore no significant influence on the catalytic activity.

Our calculation is in agreement with the result reported by Govorov *et al.* who investigated Au NPs as potential heaters. For 10 nm NPs they found a sizable temperature variation only for fluences exceeding 10³ W/cm².

References

- (1) Govorov, A. O.; Zhang, W.; Skeini, T.; Richardson, H.; Lee, J.; Kotov, N. *Nanoscale Res. Lett.* **2006**, *1*, 84.
- (2) Govorov, A. O.; Richardson, H. H. *Nano Today* **2007**, *2*, 30–38.
- (3) Van Dijk, M.; Tchegotareva, L.; Orrit, M.; Lippitz, M.; Berciaud, S.; Lasne, D.; Cognet, L.; Lounis, B. *Phys. Chem. Chem. Phys.* **2006**, *8*, 3486.